Wave propagation in viscoelastic metamaterials via added-state formulation

Andrea Arena[a,*], Andrea Bacigalupo[b], Marco Lepidi[b]

[a] *Department of Structural and Geotechnical Engineering, Sapienza University of Rome, Rome, Italy.*
[b] *Department of Civil, Chemical and Environmental Engineering, University of Genoa, Genoa, Italy.*

Abstract

Mechanical metamaterials composed of a non dissipative periodic microstructure of flexible ligaments and stiff rings, viscoelastically coupled with local resonators, are considered. By following a variational approach, the linear damped dynamics are described according to a beam lattice formulation, valid for a generic coordination number. A consistent theoretical description of the viscoelastic ring-resonator coupling is introduced, leading to an integral-differential form of the governing equations. The enlargement of the model dimension by addition of viscoelastic states allows to conveniently describe the metamaterial dynamics through a system of ordinary differential equations. Therefore, the application of the $\mathcal{Z}$-transform and a suitable mapping in the wavevector space allows to obtain the system of ordinary differential equations governing the free and forced propagation of damped waves. Subsequently, the polynomial eigenproblem ruling the harmonic free wave propagation in the complex frequency domain is stated by applying the bilateral Laplace transform, whereas an analytical procedure is outlined to solve the forced wave propagation problem in the time domain. The triangular beam lattice metamaterial is considered as significant benchmark for application of the theoretical and methodological framework. Considering first the free wave propagation, the properties of the dynamic stiffness matrix are discussed and the dispersion frequency spectrum is parametrically investigated, with focus on the spectral effects of the viscoelastic coupling. The dependence of the stop bandwidth amplitude between the low and high-frequency spectral branches on the relaxation time characterizing the viscous function is also highlighted and discussed. Moreover, the forced response to a harmonic external point source is numerically investigated in the time domain. The results are qualitatively compared and quantitatively discussed by distinguishing the fundamental cases of non-resonant, resonant and quasi-resonant excitation frequency.

Keywords: Periodic materials, Mechanical metamaterials, Beam lattices, Viscous damping, Dispersion properties, Complex band structure, Band gaps

1. Introduction

Microstructured material and metamaterial science is a fascinating and challenging field of theoretical and applied research that is continuously garnering growing attention from the scientific community of solid and structural mechanics [1, 2]. Within this engaging and promising scenario, exceptional and unprecedented progresses in the technical disciplines of high-performance supercomputing, high-fidelity microengineering, and high-precision manufacturing concur to decisively support and propel the conception and development of innovative materials with smart, unconventional or even exotic features. The primary valuable outcome of these multidisciplinary research efforts is the rapid advent and sustainable design of new engineered composites outperforming the basic physical properties of natural materials in a myriad of technical applications across all the classical and advanced branches of mechanics, including – among the others – extreme mechanics, nanomechanics, mechatronics, acoustics, thermomechanics, biomechanics [3–6].

*Andrea Arena
Email address: andrea.arena@uniroma1.it (Andrea Arena)

Within the rich variety of engineered cellular composites, the class of mechanical (or acoustic) metamaterials is characterized by a periodic architected microstructure that can be mechanically functionalized to achieve superior macroscopic effective properties, significantly outdistancing the individual performances of each ingredient material used to create the microstructured cell [7–10]. Specifically, the exceptional performances of mechanical metamaterials are made possible by the fine design of intracellular micromechanisms, which activate diffuse phenomena – like local resonances, inertia amplifications, viscoelastic metadamping – that interact with (but can also govern) the global dynamics of the cellular microstructure. Indeed, mechanical metamaterials have been successfully exploited to custom tailor several formidable or unconventional dynamic functionalities, including for instance giant hysteresis, negative indexes of dynamic refraction, nonreciprocal vibration propagation, broadband sound absorption, controllable wave guiding, obstacle cloaking, low-frequency noise filtering, energy focusing or harvesting [11–18]. According to a broader logic of multi-objective design, mechanical metamaterials can also be optimized to conjugate their dynamic functionalities with exceptional quasi-static properties, like super lightness-to-strength ratios, extra toughness, strong auxeticity, extreme thermal coefficients, vanishing shear moduli, morphing and multi-stability [19–23].

Focusing on the linear dynamics of mechanical metamaterials, a major emerging research issue of theoretical and applied interest consists in governing the free and forced wave propagation by means of optimization techniques for the spectral band structure, often supported by the micromechanical design of local energy dissipators. In the absence of dissipation, the wave propagation around certain target center-frequencies can be inhibited by finely designing the stiffness and inertia parameters of the conservative cellular microstructure, in order to open stop bands in the dispersion spectrum. Following this general idea, the spectral design can be stated either as an inverse problem or as an optimization problem. According to the former approach, the eigenproblem governing the free wave propagation can be stated, solved and – in principle – inverted to analytically assess the microstructural parameters satisfying desired spectral requirements, like the existence and position of a given harmonic spectral component or the amplitude and centerfrequency of certain pass or stop spectral bands [24, 25]. Naturally, the analytical solution of the direct and inverse eigenproblem tends to be infeasible in presence of high model dimensions, large parameter spaces or important nonlinearities, leaving space to consistent mathematical approximations, like asymptotic perturbation-based solutions [26, 27]. According to the latter approach, the optimal solution in the multidimensional space of the design parameters is numerically identified by minimizing or maximizing a suited objective or multi-objective function [28–31]. Generally, a proper mathematical surrogation of the objective function or a proper dimensionality reduction of the parameter space may help in reducing the computational costs and accelerating the algorithmic convergence [32–34]. In the presence of dissipation, the mechanical energy trapped by the propagation-inhibiting local mechanisms is irreversibly absorbed by dampers or – if convenient – extracted by harvesters. In this respect, the spectral design of dissipative metamaterials poses serious conceptual and methodological challenges, including for instance (i) the enlargement of the parameter space, extended to embrace the dissipation properties of the dampers or harvesters, (ii) the non-standard (e.g. non-polynomial) nature of the eigenproblem governing the dispersion problem, if some common viscoelastic formulations are adopted, (iii) the complexification of the dispersion relations defining the frequency spectrum, in which the number of frequency-wavevector curves can also exceed the model dimension, due to the presence of pure attenuation branches associated to standing damped waveforms, (iv) the role played by geometrical and constitutive nonlinearities, which may become crucial if the oscillation amplitudes require to be maximized to enlarge the hysteresis cycles or improve the efficiency of the energy conversion [35]. This entire motivating background can be efficiently synthesized by recognizing that a systematic improvement in the description of the linear and nonlinear dissipation phenomena is the milestone for planning future advances in the energetically consistent modelization and spectral design of mechanical metamaterials [3, 36]. According to a broader vision, it could be postulated that in the next few years a completely new generation of mechanical meta-behaviors will emerge, exploiting the virtuous contrast and collaborative synergy between constituent materials and ingredients characterized by highly dissimilar elastic, plastic and viscous properties [20].

Based on these motivations, the paper presents a beam lattice formulation governing the free and forced wave propagation in a mechanical metamaterial, originated by viscoelastically coupling a periodic non dissipative microstructure of flexible ligaments and stiff rings with local tunable resonators. As original aspect, the mechanical model is formulated according to a variational strategy for a generic coordination number.

The viscoelastic coupling is consistently derived by a physical-mathematical description based on the Boltzmann superposition integral [37], whose kernel is approximable by a Prony series [38–41]. Accordingly, the dissipative forces are defined in terms of the past history, and not only on the instantaneous values, of generalized velocities via convolution of suitable kernel functions [42]. The integral description of the viscoelastic dissipation enriches and includes (as particular cases) other classic formulations of viscous damping in mechanical metamaterials, mostly based on the rheological Rayleigh, Maxwell or Wiechert models [43–45]. According to the model assumptions, the free and forced damped dynamics of the mechanical metamaterial is governed by a linear system of coupled integro-differential equations of motion. As complementary original aspect, the differentiation properties of the N exponential functions in the Prony series are leveraged to reformulate the dynamic model in an enlarged state space, including N additional viscoelastic variables. The essential and valuable consequence is that the free and forced damped dynamics turns out to be described by a coupled system of ordinary differential equations providing a straightforward state-space representation suitable for the characterization and the study of non-viscously damped systems, as also shown in [46] and, more recently, in [47]. Interestingly, the proposed mathematical formulation describing the viscoelastic behavior of internal resonators finds a strong similarity with the so-called indicial function theory adopted in aerodynamics. Within this theory, the time evolution of the aerodynamic forces is described by the convolution integral of specific functions representing the response of a lifting surface to the instantaneous variation of an aerodynamic input. As for the case of viscoelasticity, the kernel functions can have several expressions, as exponential series or polynomial fractions. This general theory for the formulation of aerodynamic loads was first developed by [48] and studied by [49, 50] and, then, well illustrated in [51, 52]; finally, it found several applications in the aeroelasticity of aircraft wings [53] and suspension bridges [54].

Back to the description of the present study, after application of the Laplace and $\mathcal{Z}$ transforms to deal with the time and space periodicity, the free propagation of damped harmonic waves is governed by a polynomial algebraic eigenproblem. In this respect, enlarging the state space can be deemed a profitable methodological advance that allows to circumvent the algorithmic complexities of de-rationalizing or asymptotically approximating the characteristic equation [55, 56]. Therefore, according to the so-called inverse method [3], the eigenproblem is solved in the space of complex-valued frequencies for varying real-valued wavevectors to determine the dispersion spectrum. Concerning the supplementary dynamic problem of forced wave propagation, a general procedure is outlined to achieve the analytical solution in the time domain, thus complementing the solution scheme already outlined in the frequency domain, based on the evaluation of the dynamic compliance matrix [56].

The paper is organized as follows. First, the general conceptual framework introduced above, concerning both the physical-mathematical models of mechanical metamaterials and the methodological tools necessary to treat the governing equations, is presented (Sections 2 and 3). Second, the entire formulation is specialized for the triangular beam lattice metamaterial (Section 4). The free wave propagation is investigated by discussing a priori the properties of the dynamic stiffness matrix and by subsequently analyzing the dispersion properties (wavefrequencies and waveforms) and their parametric dependence on the viscoelastic parameters (Section 5). Therefore, the forced response to a harmonic mono-frequent external point source is investigated in the time domain for the fundamental cases of non-resonant, resonant and quasi-resonant excitation frequency (Section 6). Finally, concluding remarks are pointed out.

2. Mechanical formulation

An architected metamaterial characterized by a cellular microstructure, topologically based on an periodic and regular tessellation of the infinite two-dimensional domain, is considered (Fig. 1a). The composite centrosymmetric microstructure of the periodic cell is featured by a central heavy and stiff ring, with mean radius R. The nearest-neighborhood intercellular interactions are mechanically provided by n identical light, flexible and slender ligaments, with length L, radially connecting the central ring to the rings of the adjacent cells (Fig. 1b). The even number $n \in \mathbb{N}$ can be referred to as *coordination number* of the periodic microstructure, adopting the nomenclature of molecular crystallography. According to a beam lattice formulation, the ring is modeled as a perfectly rigid massive body, with mass M, while the ligaments are described as elastic

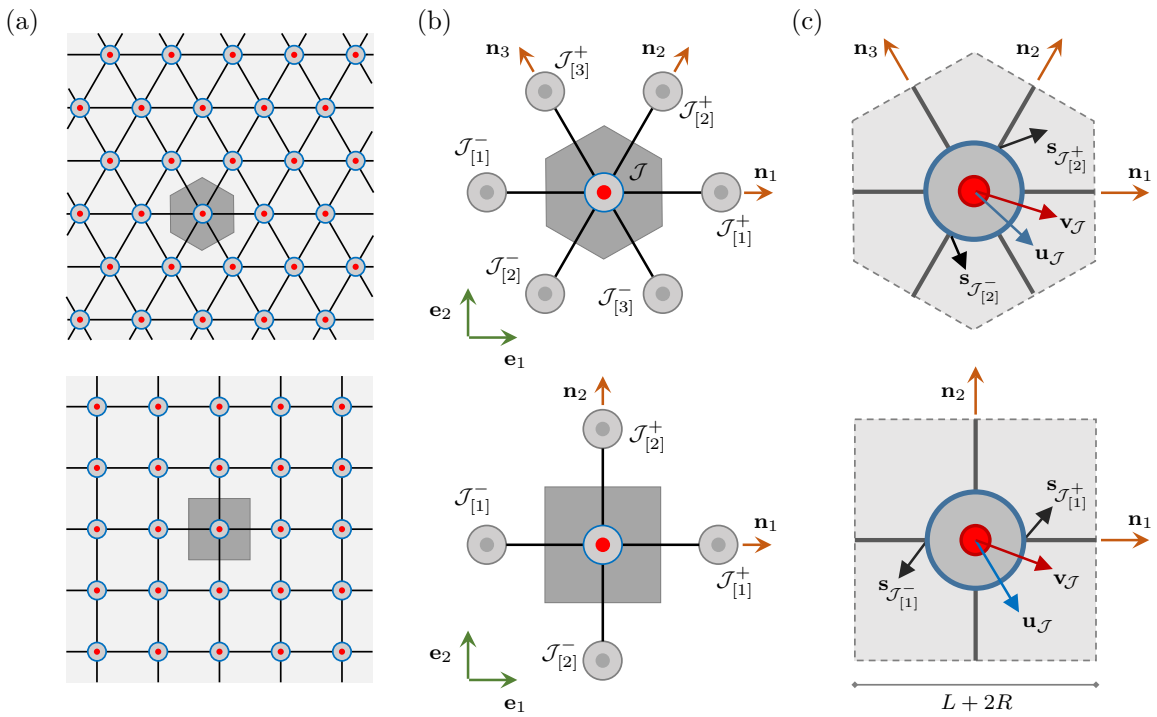

Figure 1: Architected metamaterials with triangular (top) and quadrilateral (bottom) cellular topologies: (a) regular tessellation of the infinite two-dimensional domain, (b) periodic cell, coordination ways and directions, (c) microstructural lattice model.

unshearable massless beams with axial stiffness EA and bending stiffness EJ (Fig. 1c). In order to realize a *mechanical*, or *acoustic* metamaterial, a co-centric stiff micro-disk, with radius $R_r < R$, is included in each ring, embedded in an annular deformable matrix made of viscoelastic material. The inclusions, modeled as perfectly rigid circular bodies with mass M_r, play the role of damped local resonators able at exchanging energy with the embedding periodic microstructure.

The linear kinematics of the system can conveniently be described by introducing the canonical basis $\{\mathbf{e}_1, \mathbf{e}_2, \mathbf{e}_3\}$, where $(\mathbf{e}_1, \mathbf{e}_2)$ is the plane containing the metamaterial and $\mathbf{e}_3$ is the out-of-plane direction. The set $\mathcal{J} = (i_1, ..., i_{n/2})$ collects the indexes spanning the $n/2$ unique coordination ways, each identified by the unit vector $\mathbf{n}_j$ (with $j = 1, ..., n/2$). A particular cell is univocally identified by fixing all the independent indexes of the set $\mathcal{J}$. The increment or decrement of the index i_j allow the univocal identification of the adjacent cells along the positive and negative directions of the i_j-th coordination way, indexed by the sets $\mathcal{J}^+_{[j]} = (i_1, ..., i_j + 1, ..., i_{n/2})$ and $\mathcal{J}^-_{[j]} = (i_1, ..., i_j - 1, ..., i_{n/2})$, respectively. As long as iso-length ligaments are considered, the unit vectors $\mathbf{n}_j$ are univocally defined by assigning the coordination number n, by virtue of geometrical considerations. Within this context, the dynamic configuration of the $\mathcal{J}$-th cell is described by the kinematic descriptors of the $\mathcal{J}$-th ring and the $\mathcal{J}$-th inclusion, defined through the 3-by-1 vectors $\mathbf{u}_{\mathcal{J}} = [U, V, \phi]^\top_{\mathcal{J}}$ and $\mathbf{v}_{\mathcal{J}} = [U_r, V_r, \phi_r]^\top_{\mathcal{J}}$, respectively, where superscript $\top$ indicates the transpose operator. In particular, the components U, V represent the in-plane displacements of the ring centroid along the direction $\mathbf{e}_1$ and $\mathbf{e}_2$, respectively, while ϕ is the ring rotation about the axis $\mathbf{e}_3$. On the other hand, the components U_r, V_r, and ϕ_r are the centroidal displacements along $\mathbf{e}_1$ and $\mathbf{e}_2$, and the rotation about $\mathbf{e}_3$, respectively, of the $\mathcal{J}$-th rigid inclusion. It is worth remarking that, in the reference natural configuration, the set of configurational nodes of the mechanical metamaterial univocally corresponds with a two-dimensional lattice of geometric points with $n/2$ periodicity vectors $\mathbf{d}_j$.

According to a variational approach for the statement of the ordinary differential equations of motion governing the beam lattice model, the kinetic energy of the $\mathcal{J}$-th cell can be expressed as a quadratic function

of the ring and resonator velocity vectors

$$\mathcal{T}_{\mathcal{J}} = \tfrac{1}{2}\dot{\mathbf{u}}_{\mathcal{J}}^{\top}\mathbf{M}\,\dot{\mathbf{u}}_{\mathcal{J}} + \tfrac{1}{2}\dot{\mathbf{v}}_{\mathcal{J}}^{\top}\mathbf{M}_r\dot{\mathbf{v}}_{\mathcal{J}} \tag{1}$$

where dot indicates differentiation with respect to the time t, while $\mathbf{M} = \mathrm{diag}(M, M, MR^2)$ and $\mathbf{M}_r = \mathrm{diag}(M_r, M_r, \frac{1}{2}M_rR_r^2)$ represent the 3-by-3 diagonal mass matrices of the ring and the resonator, respectively.

The intercellular non-dissipative interactions between the $\mathcal{J}$-th cell and the adjacent cells are governed by the 6-by-6 elastic stiffness matrix $\mathbf{K}$ of the unshearable beams connecting the respective central rings. Specifically, the elastic potential energy developed by the n beams connected to the ring of the $\mathcal{J}$-th cell can be expressed as a quadratic function of the nodal beam displacements

$$\mathcal{U}_{\mathcal{J}} = \tfrac{1}{2}\sum_{j=1}^{n/2}\mathbf{a}_{\mathcal{J}^-_{[j]}}^{\top}\mathbf{K}\,\mathbf{a}_{\mathcal{J}^-_{[j]}} + \tfrac{1}{2}\sum_{j=1}^{n/2}\mathbf{a}_{\mathcal{J}^+_{[j]}}^{\top}\mathbf{K}\,\mathbf{a}_{\mathcal{J}^+_{[j]}} \tag{2}$$

where the 6-by-1 vectors $\mathbf{a}_{\mathcal{J}^-_{[j]}}$ and $\mathbf{a}_{\mathcal{J}^+_{[j]}}$ collect columnwise the nodal displacements (whose components are referred to the local basis of the beam-aligned reference system) of the two beams aligned along the j-th coordination way and connecting the ordered $(\mathcal{J}^-_{[j]}, \mathcal{J})$-pair and $(\mathcal{J}, \mathcal{J}^+_{[j]})$-pair of rings, respectively. The components of the nodal displacement vectors can be expressed in the canonical reference system by applying the change-of-basis relations $\mathbf{a}_{\mathcal{J}^-_{[j]}} = \mathbf{\Theta}_j\mathbf{s}_{\mathcal{J}^-_{[j]}}$ and $\mathbf{a}_{\mathcal{J}^+_{[j]}} = \mathbf{\Theta}_j\mathbf{s}_{\mathcal{J}^+_{[j]}}$. Therefore, the elastic potential energy becomes

$$\mathcal{U}_{\mathcal{J}} = \tfrac{1}{2}\sum_{j=1}^{n/2}\mathbf{s}_{\mathcal{J}^-_{[j]}}^{\top}\mathbf{\Theta}_j^{\top}\mathbf{K}\mathbf{\Theta}_j\mathbf{s}_{\mathcal{J}^-_{[j]}} + \tfrac{1}{2}\sum_{j=1}^{n/2}\mathbf{s}_{\mathcal{J}^+_{[j]}}^{\top}\mathbf{\Theta}_j^{\top}\mathbf{K}\mathbf{\Theta}_j\mathbf{s}_{\mathcal{J}^+_{[j]}} \tag{3}$$

being the change-of-basis 6-by-6 matrix $\mathbf{\Theta}_j = \mathrm{diag}(\mathbf{R}_j^{\top}, \mathbf{R}_j^{\top})$, where

$$\mathbf{R}_j = \begin{bmatrix} \mathbf{e}_1\cdot\mathbf{n}_j & -(\mathbf{e}_1\times\mathbf{n}_j)\cdot\mathbf{e}_3 & 0 \\ (\mathbf{e}_1\times\mathbf{n}_j)\cdot\mathbf{e}_3 & \mathbf{e}_1\cdot\mathbf{n}_j & 0 \\ 0 & 0 & 1 \end{bmatrix} \tag{4}$$

is also the 3-by-3 rotation matrix rotating the canonical basis into the local basis of the $\mathbf{n}_j$-aligned beams. Assuming perfectly rigid ring-beam connections, the nodal displacement vectors can be constrained to the centroidal ring displacements by the linear relations

$$\mathbf{s}_{\mathcal{J}^-_{[j]}} = \mathbf{B}_j^-\mathbf{u}_{\mathcal{J}^-_{[j]}} + \mathbf{B}_j^+\mathbf{u}_{\mathcal{J}}, \qquad \mathbf{s}_{\mathcal{J}^+_{[j]}} = \mathbf{B}_j^-\mathbf{u}_{\mathcal{J}} + \mathbf{B}_j^+\mathbf{u}_{\mathcal{J}^+_{[j]}} \tag{5}$$

where the 6-by-3 constraining matrices $\mathbf{B}_j^+$ and $\mathbf{B}_j^-$ are

$$\mathbf{B}_j^+ = \begin{bmatrix} \mathbf{I}+\mathbf{X}_j \\ \mathbf{O} \end{bmatrix}, \qquad \mathbf{B}_j^- = \begin{bmatrix} \mathbf{O} \\ \mathbf{I}-\mathbf{X}_j \end{bmatrix} \tag{6}$$

where $\mathbf{I}$ and $\mathbf{O}$ are the 3-by-3 identity and zero matrices, respectively, while $\mathbf{X}_j = R\,(\mathbf{e}_3\times\mathbf{n}_j)\otimes\mathbf{e}_3$, being $\times$ the cross product and $\otimes$ the tensor product. By introducing the constraint relations (5), the potential elastic energy can be expressed in the compact form

$$\mathcal{U}_{\mathcal{J}} = \tfrac{1}{2}\mathbf{u}_{\mathcal{J}}^{\top}\mathbf{K}^{-}\mathbf{u}_{\mathcal{J}} + \tfrac{1}{2}\mathbf{u}_{\mathcal{J}}^{\top}\mathbf{K}^{+}\mathbf{u}_{\mathcal{J}} + \mathbf{u}_{\mathcal{J}}^{\top}\mathbf{r}_{\mathcal{J}}^{-} + \mathbf{u}_{\mathcal{J}}^{\top}\mathbf{r}_{\mathcal{J}}^{+} + \mathcal{U}_{\mathcal{J}}^{-} + \mathcal{U}_{\mathcal{J}}^{+} \tag{7}$$

where $\mathbf{K}^-$ and $\mathbf{K}^+$ are the 3-by-3 global stiffness matrices accounting for the beams connected to the ring of the $\mathcal{J}$-th cell and aligned along the positive and negative directions of the i_j-th coordination way

$$\mathbf{K}^- = \sum_{j=1}^{n/2}(\mathbf{B}_j^-)^{\top}\mathbf{\Theta}_j^{\top}\mathbf{K}\,\mathbf{\Theta}_j\,\mathbf{B}_j^-, \qquad \mathbf{K}^+ = \sum_{j=1}^{n/2}(\mathbf{B}_j^+)^{\top}\mathbf{\Theta}_j^{\top}\mathbf{K}\,\mathbf{\Theta}_j\,\mathbf{B}_j^+ \tag{8}$$

and $\mathbf{r}^-_{\mathcal{J}}$ and $\mathbf{r}^+_{\mathcal{J}}$ are the $\mathbb{R}^3$ vectors collecting columwise the intercellular forces exerted at the centroid of the $\mathcal{J}$-th cell by the adjacent cells

$$\mathbf{r}^-_{\mathcal{J}} = \sum_{j=1}^{n/2} (\mathbf{B}^+_j)^\top \boldsymbol{\Theta}_j^\top \mathbf{K}\, \boldsymbol{\Theta}_j\, \mathbf{B}^-_j \mathbf{u}_{\mathcal{J}^-_{[j]}}, \qquad \mathbf{r}^+_{\mathcal{J}} = \sum_{j=1}^{n/2} (\mathbf{B}^-_j)^\top \boldsymbol{\Theta}_j^\top \mathbf{K}\, \boldsymbol{\Theta}_j\, \mathbf{B}^+_j \mathbf{u}_{\mathcal{J}^+_{[j]}} \tag{9}$$

while the $\mathbf{u}_{\mathcal{J}}$-independent terms

$$\mathcal{U}^-_{\mathcal{J}} = \tfrac{1}{2} \sum_{j=1}^{n/2} \mathbf{u}^\top_{\mathcal{J}^-_{[j]}} (\mathbf{B}^-_j)^\top \boldsymbol{\Theta}_j^\top \mathbf{K}\, \boldsymbol{\Theta}_j\, \mathbf{B}^-_j \mathbf{u}_{\mathcal{J}^-_{[j]}}, \qquad \mathcal{U}^+_{\mathcal{J}} = \tfrac{1}{2} \sum_{j=1}^{n/2} \mathbf{u}^\top_{\mathcal{J}^+_{[j]}} (\mathbf{B}^+_j)^\top \boldsymbol{\Theta}_j^\top \mathbf{K}\, \boldsymbol{\Theta}_j\, \mathbf{B}^+_j \mathbf{u}_{\mathcal{J}^+_{[j]}} \tag{10}$$

represent the contributions to the potential energy of the adjacent cells.

The intracellular dissipative interaction in the $\mathcal{J}$-th cell microstructure is governed by a linear constitutive law expressing the $\mathbb{R}^3$ vector $\mathbf{g}_{\mathcal{J}}(t)$ of internal forces exchanged between the ring and the resonator. The constitutive law is intended to synthetically describe the viscoelastic behavior of the intra-ring resonator-embedding matrix by coupling the displacement vectors of the ring and the resonator according to the convolution relationship

$$\mathbf{g}_{\mathcal{J}}(t) = \int_{-\infty}^{t} \mathbf{G}(t - t_*) \frac{\partial}{\partial t_*} \Big(\mathbf{u}_{\mathcal{J}}(t_*) - \mathbf{v}_{\mathcal{J}}(t_*) \Big)\, dt_*, \tag{11}$$

where t_* indicates an auxiliary time variable and the time-dependent 3-by-3 viscoelastic diagonal kernel collects the viscous relaxation functions. Employing the Prony series to express the relaxation functions and considering only the first term (corresponding to infinite relaxation time) and lowest N terms (each of them corresponding to a finite relaxation time $t_{r,k}$) of the series, the viscoelastic kernel reads

$$\mathbf{G}(t) = \operatorname{diag}\left(k_U \Big(1 + \sum_{k=1}^{N} \beta_{U,k}\, e^{-t/t_{r,k}}\Big), k_V \Big(1 + \sum_{k=1}^{N} \beta_{V,k}\, e^{-t/t_{r,k}}\Big), k_\phi \Big(1 + \sum_{k=1}^{N} \beta_{\phi,k}\, e^{-t/t_{r,k}}\Big) \right), \tag{12}$$

where the positive nondimensional coefficients $\beta_{U,k}$, $\beta_{V,k}$, $\beta_{\phi,k}$ can be referred to as *viscosity ratios* for the kth relaxation time $t_{r,k}$. By assuming – without loss of generality – that the motion starts at time $t = 0$, the difference $\mathbf{u}_{\mathcal{J}}(t_*) - \mathbf{v}_{\mathcal{J}}(t_*) = \mathbf{0}$ for $t < 0$, being $\mathbf{G}(t - t_*) = \mathbf{O}$ for $t < t_*$ (i.e. considering $\mathbf{G}(t)$ a *causal function*). Therefore, integrating by part, Eq. (11) becomes

$$\mathbf{g}_{\mathcal{J}}(t) = \mathbf{G}_0 \Big(\mathbf{u}_{\mathcal{J}}(t) - \mathbf{v}_{\mathcal{J}}(t) \Big) - \int_0^t \frac{\partial}{\partial t_*} \mathbf{G}(t - t_*) \Big(\mathbf{u}_{\mathcal{J}}(t_*) - \mathbf{v}_{\mathcal{J}}(t_*) \Big)\, dt_*, \tag{13}$$

where $\mathbf{G}_0 = \mathbf{G}(0)$ can conveniently be written as $\mathbf{G}_0 = (\mathbf{I} + \mathbf{S})\mathbf{K}_e$, with $\mathbf{I}$ being the 3-by-3 identity matrix, $\mathbf{S} = \sum_{k=1}^{N} \mathbf{D}_k$, while $\mathbf{K}_e$ and $\mathbf{D}_k$ are diagonal matrices defined as:

$$\mathbf{K}_e = \operatorname{diag}(k_U, k_V, k_\phi), \qquad \mathbf{D}_k = \operatorname{diag}(\beta_{U,k}, \beta_{V,k}, \beta_{\phi,k}). \tag{14}$$

The matrix $\mathbf{K}_e$ is related to the elastic part of the intracellular coupling, while $\mathbf{D}_k$ represents the viscous part associated with the kth term of the Prony series. Specifically, the two mechanical limit cases of (different) undamped metamaterials, characterized by purely elastic resonators, are recovered for: (i) infinite relaxation time $t_{r,k} \to +\infty$ corresponding to $\mathbf{G}(t) = \mathbf{G}_0$ (*stiffer* undamped metamaterial) or (ii) absence of viscosity, realizable by null viscosity ratios $\mathbf{S} = \mathbf{O}$ and/or vanishing relaxation time $t_{r,k} \to 0^+$ (*softer* undamped metamaterial). By invoking the differentiation properties of the exponential functions present in Eq. (12), and introducing the kth vector $\mathbf{w}_k(t) = [W_{U,k}\, W_{V,k}\, W_{\phi,k}]^\top$ collecting additional viscoelastic states, Eq. (13) can be re-written in the form

$$\mathbf{g}_{\mathcal{J}}(t) = (\mathbf{I} + \mathbf{S})\, \mathbf{K}_e \Big(\mathbf{u}_{\mathcal{J}}(t) - \mathbf{v}_{\mathcal{J}}(t) \Big) - \sum_{k=1}^{N} \mathbf{T}_k\, \mathbf{D}_k\, \mathbf{K}_e \mathbf{w}_k(t), \tag{15}$$

which is featured by time-independent coefficients (all details of the formulation are reported in the Appendix A). For consistency, Eq. (15) is complemented by the N first-order evolutionary vector-valued equations governing the dynamics of the added viscoelastic states

$$\dot{\mathbf{w}}_k(t) + \mathbf{T}_k\,\mathbf{w}_k(t) - \big(\mathbf{u}_{\mathcal{J}}(t) - \mathbf{v}_{\mathcal{J}}(t)\big) = \mathbf{0} \quad (k = 1, \dots, N), \tag{16}$$

where $\mathbf{T}_k$ is a diagonal matrix collecting the inverse of the kth relaxation time as $\mathbf{T}_k = t_{r,k}^{-1}\,\mathbf{I}$.

By introducing the internal work $\mathcal{V}_{\mathcal{J}} = (\mathbf{u}_{\mathcal{J}} - \mathbf{v}_{\mathcal{J}})^{\top}\mathbf{g}_{\mathcal{J}}$ done by the viscoelastic intracellular force $\mathbf{g}_{\mathcal{J}}$ and accounting for the external work $\mathcal{W}_{\mathcal{J}} = \mathbf{u}_{\mathcal{J}}^{\top}\mathbf{f}_{\mathcal{J}}$ done by the $\mathbb{R}^3$ vector $\mathbf{f}_{\mathcal{J}} = [F_U, F_V, F_\phi]_{\mathcal{J}}^{\top}$ of external excitation acting on the ring (whereas the resonator is considered unloaded), the functional $\mathcal{H}_{\mathcal{J}}$ representing the generalized Hamiltonian action can be formulated as

$$\mathcal{H}_{\mathcal{J}} = \int_{t_1}^{t_2} \left(\mathcal{T}_{\mathcal{J}} - \mathcal{U}_{\mathcal{J}} - \mathcal{V}_{\mathcal{J}} + \mathcal{W}_{\mathcal{J}}\right) \mathrm{d}t \tag{17}$$

and its variation with respect to all (and only) the configuration variables of the $\mathcal{J}$-the cell reads

$$\delta\mathcal{H}_{\mathcal{J}} = \int_{t_1}^{t_2} \left[\delta\dot{\mathbf{u}}_{\mathcal{J}}^{\top}\mathbf{M}\dot{\mathbf{u}}_{\mathcal{J}} - \delta\mathbf{u}_{\mathcal{J}}^{\top}\left(\mathbf{K}^{-}\mathbf{u}_{\mathcal{J}} + \mathbf{K}^{+}\mathbf{u}_{\mathcal{J}} + \mathbf{r}_{\mathcal{J}}^{+} + \mathbf{r}_{\mathcal{J}}^{-} + \mathbf{g}_{\mathcal{J}} - \mathbf{f}_{\mathcal{J}}\right) + \delta\dot{\mathbf{v}}_{\mathcal{J}}^{\top}\mathbf{M}_r\dot{\mathbf{v}}_{\mathcal{J}} + \delta\mathbf{v}_{\mathcal{J}}^{\top}\mathbf{g}_{\mathcal{J}}\right] \mathrm{d}t. \tag{18}$$

Therefore, integrating by parts the contributions of the varied kinetic energy and imposing the stationarity condition $\delta\mathcal{H}_{\mathcal{J}} = 0$, $\forall\delta\mathbf{u}_{\mathcal{J}}$, $\forall\delta\mathbf{v}_{\mathcal{J}}$, the coupled linear system of ordinary differential equations governing the forced damped dynamics of the $\mathcal{J}$-th periodic cell are obtained

$$\begin{aligned} &\mathbf{M}\ddot{\mathbf{u}}_{\mathcal{J}} + \mathbf{K}^{-}\mathbf{u}_{\mathcal{J}} + \mathbf{K}^{+}\mathbf{u}_{\mathcal{J}} + \mathbf{r}_{\mathcal{J}}^{+} + \mathbf{r}_{\mathcal{J}}^{-} + \mathbf{g}_{\mathcal{J}} = \mathbf{f}_{\mathcal{J}}, \\ &\mathbf{M}_r\ddot{\mathbf{v}}_{\mathcal{J}} - \mathbf{g}_{\mathcal{J}} = \mathbf{0}, \end{aligned} \tag{19}$$

where the first equation governs the motion of the central ring, the second equation governs the motion of the resonator, and the coupling term $\mathbf{g}_{\mathcal{J}}$ is given by Eq. (15) together with the system of evolutionary equations of the N additional viscoelastic states whose kth component is given by Eq. (16). Finally, natural initial conditions are assigned to represent the dynamical state at time $t = 0$.

As conclusive remark, it may be worth noting that the variational formulation leading to Eqs. (19) is effectively general. This consideration means that – once the mass matrices $\mathbf{M}$ and $\mathbf{M}_r$, the stiffness matrix $\mathbf{K}$ and the viscoelastic matrices $\mathbf{K}_e$, $\mathbf{S}$ and $\mathbf{T}_k$ are defined – assigning just the coordination number n is sufficient to formulate the equations of motion for the corresponding beam lattice metamaterial (say $n = 4$ or $n = 6$ for the quadrilateral or triangular metamaterials illustrated in Fig. 1, respectively).

3. Damped Bloch wave propagation

The time-differential equation (19a) can be considered as a non-homogeneous linear space-difference equation in the iterates of the variable $\mathbf{u}_{\mathcal{J}}$, governing the elasto-dynamic interactions of the generic $\mathcal{J}$-th periodic cell with its nearest neighborhoods. An efficient methodological strategy to solve this kind of mechanical problems involving spatial periodicity consists in using the bilateral $\mathcal{Z}$ transform, which applies to the generic m-dimensional vector-valued sequence $\mathbf{y}_{\mathcal{J}} : \mathbb{Z}^{n/2} \to \mathbb{C}^m$ as the product of $n/2$ infinite summations

$$\mathcal{Z}[\mathbf{y}_{\mathcal{J}}] = \mathcal{Z}[\mathbf{y}_{(i_1,\dots,i_{n/2})}] = \sum_{i_1=-\infty}^{\infty} \cdots \sum_{i_{n/2}=-\infty}^{\infty} \mathbf{y}_{(i_1,\dots,i_{n/2})} z_1^{-i_1} \dots z_{n/2}^{-i_{n/2}} =: \mathring{\mathbf{y}}(\mathbf{z}) \tag{20}$$

where the variable $\mathbf{z} \in \mathbb{C}^{n/2}$ and the transformed variable $\mathring{\mathbf{y}}(\mathbf{z}) : \mathbb{C}^{n/2} \to \mathbb{C}^m$. As profitable consequence, the $\mathcal{Z}$-transforms of the intercellular vector forces $\mathbf{r}_{\mathcal{J}}^{-}$ and $\mathbf{r}_{\mathcal{J}}^{+}$, depending on the j-incremented and j-decremented variables $\mathbf{u}_{\mathcal{J}_{[j]}^{-}}$ and $\mathbf{u}_{\mathcal{J}_{[j]}^{+}}$, can be expressed as $\mathring{\mathbf{u}}(\mathbf{z})$-dependent variables

$$\mathring{\mathbf{r}}^{-}(\mathbf{z}) = \Big(\sum_{j=1}^{n/2} z_j^{-1}{\mathbf{B}_j^{-}}^{\top}\mathbf{\Theta}_j^{\top}\mathbf{K}\,\mathbf{\Theta}_j\,\mathbf{B}_j^{+}\Big)\mathring{\mathbf{u}}(\mathbf{z}), \qquad \mathring{\mathbf{r}}^{+}(\mathbf{z}) = \Big(\sum_{j=1}^{n/2} z_j{\mathbf{B}_j^{+}}^{\top}\mathbf{\Theta}_j^{\top}\mathbf{K}\,\mathbf{\Theta}_j\,\mathbf{B}_j^{-}\Big)\mathring{\mathbf{u}}(\mathbf{z}), \tag{21}$$

where the shifting property of the bilateral $\mathcal{Z}$ transform $\mathcal{Z}[\mathbf{y}_{(i_1\pm k_1,\ldots,i_{n/2}\pm k_{n/2})}] = z^{\pm k_1}\ldots z^{\pm k_{n/2}}\mathcal{Z}[\mathbf{y}_{(i_i,\ldots i_{n/2})}]$ has been conveniently invoked. Therefore, the ordinary differential equations of motion governing the forced dynamics of the periodic beam lattice metamaterial can be expressed in $\mathcal{Z}$ transformed variables as

$$\begin{aligned}
&\mathbf{M}(\mathring{\mathbf{u}}(\mathbf{z}))^{\cdot\cdot} + (\mathbf{I}+\mathbf{S})\,\mathbf{K}_e\Big(\mathring{\mathbf{u}}(\mathbf{z}) - \mathring{\mathbf{v}}(\mathbf{z})\Big) + \mathbf{H}(\mathbf{z})\mathring{\mathbf{u}}(\mathbf{z}) - \sum_{k=1}^{N}\mathbf{T}_k\,\mathbf{D}_k\,\mathbf{K}_e\mathring{\mathbf{w}}_k(\mathbf{z}) = \mathring{\mathbf{f}}(\mathbf{z}), \\
&\mathbf{M}_r(\mathring{\mathbf{v}}(\mathbf{z}))^{\cdot\cdot} - (\mathbf{I}+\mathbf{S})\,\mathbf{K}_e\Big(\mathring{\mathbf{u}}(\mathbf{z}) - \mathring{\mathbf{v}}(\mathbf{z})\Big) + \sum_{k=1}^{N}\mathbf{T}_k\,\mathbf{D}_k\,\mathbf{K}_e\mathring{\mathbf{w}}_k(\mathbf{z}) = \mathbf{0}, \\
&(\mathring{\mathbf{w}}_k(\mathbf{z}))^{\cdot} + \mathbf{T}_k\,\mathring{\mathbf{w}}_k(\mathbf{z}) - \Big(\mathring{\mathbf{u}}(\mathbf{z}) - \mathring{\mathbf{v}}(\mathbf{z})\Big) = \mathbf{0} \qquad (k = 1\ldots, N),
\end{aligned} \tag{22}$$

where the 3-by-3 Hermitian matrix

$$\mathbf{H}(\mathbf{z}) = \mathbf{K}^- + \mathbf{K}^+ + \sum_{j=1}^{n/2} z_j^{-1}(\mathbf{B}_j^-)^\top\mathbf{\Theta}_j^\top\mathbf{K}\,\mathbf{\Theta}_j\,\mathbf{B}_j^+ + \sum_{j=1}^{n/2} z_j(\mathbf{B}_j^+)^\top\mathbf{\Theta}_j^\top\mathbf{K}\,\mathbf{\Theta}_j\,\mathbf{B}_j^-, \tag{23}$$

is the generalized $\mathbf{z}$-dependent stiffness matrix governing the resonator-free periodic material in the transformed $\mathcal{Z}$-space. Furthermore, the complex-valued variables z_j can be continuously mapped in the unitary circle according to the relation $z_j = \exp(\imath\, B\mathbf{n}_j\cdot\mathbf{k})$, where $\imath$ is the imaginary unit and $B = L + 2R$ is the internodal distance between the lattice nodes. It is worth remarking that, since the mapped $\mathcal{Z}$-space coincides with the reciprocal space, the vector variable $\mathbf{k} = [k_1, k_2, 0]^\top$ can play the role of wavevector for the reciprocal lattice. By collecting the kinematic descriptors and the additional viscoelastic states into the $(6{+}3N)$-by-1 vector $\mathbf{q}(t) = [\mathbf{u}_\mathcal{J}, \mathbf{v}_\mathcal{J}, \ldots, \mathbf{w}_N]$, and introducing the $(6{+}3N)$-by-1 vector $\mathbf{p}(t) = [\mathbf{f}_\mathcal{J}, \mathbf{0}, \ldots \mathbf{0}_N]$ of the generalized forces, where $\mathbf{0}$ and $\mathbf{0}_N$ are 3-by-1 zero vectors, the $\mathcal{Z}$-transformed counterparts of these vectors can be defined as $\mathring{\mathbf{q}}(t,\mathbf{k}) = \mathcal{Z}[\mathbf{q}(t)]|_{z_j=\exp(\imath\, B\mathbf{n}_j\cdot\mathbf{k})}$ and $\mathring{\mathbf{p}}(t,\mathbf{k}) = \mathcal{Z}[\mathbf{p}(t)]|_{z_j=\exp(\imath\, B\mathbf{n}_j\cdot\mathbf{k})}$, respectively. Then, the equations of motion (22) can be expressed in the compact form

$$\tilde{\mathbf{M}}(\mathring{\mathbf{q}}(t,\mathbf{k}))^{\cdot\cdot} + \tilde{\mathbf{Y}}(\mathring{\mathbf{q}}(t,\mathbf{k}))^{\cdot} + \tilde{\mathbf{K}}(\mathbf{k})\,\mathring{\mathbf{q}}(t,\mathbf{k}) = \mathring{\mathbf{p}}(t,\mathbf{k}), \tag{24}$$

where the augmented $(6+3N)$-by-$(6+3N)$ mass matrix $\tilde{\mathbf{M}} = \mathrm{diag}(\mathbf{M}, \mathbf{M}_r, \mathbf{O}, ..., \mathbf{O}_N)$ and the augmented $(6{+}3N)$-by-$(6{+}3N)$ matrix $\tilde{\mathbf{Y}} = \mathrm{diag}(\mathbf{O}, \mathbf{O}, \mathbf{I}, ..., \mathbf{I}_N)$. Finally, the augmented $(6{+}3N)$-by-$(6{+}3N)$ stiffness matrix $\tilde{\mathbf{K}}$ is non-symmetric, $\mathbf{k}$-dependent and reported in the Appendix B.

The dynamic system (24) can be solved directly in the time domain, according to the analytical procedure outlined in the Appendix C. Alternately, it may be convenient to re-formulate the equations of motion in the frequency domain. To this purpose, the $\mathbf{k}$-mapped $\mathcal{Z}$-transformed variables in the Eqs.(24) can be treated by applying the bilateral Laplace transform, which applies to the generic m-dimensional time-dependent vector variable $\mathring{\mathbf{y}}(t) : \mathbb{C} \to \mathbb{C}^m$ as the integral

$$\mathcal{L}[\mathring{\mathbf{y}}(t)] = \int_{-\infty}^{\infty}\mathring{\mathbf{y}}(t)\exp(-st)\mathrm{d}t =: \hat{\mathbf{y}}(s), \tag{25}$$

where $s \in \mathbb{C}$ is the Laplace variable and the transformed variable $\hat{\mathbf{y}}(s) : \mathbb{C} \to \mathbb{C}^m$. Consequently, the ordinary differential equations of motion (22) can be re-formulated as algebraic equations in the compact form

$$\mathbf{L}(s,\mathbf{k})\hat{\mathbf{q}}(s,\mathbf{k}) = \hat{\mathbf{p}}(s,\mathbf{k}), \tag{26}$$

where $\hat{\mathbf{q}}(s,\mathbf{k}) = \mathcal{L}[\mathring{\mathbf{q}}]$ and $\hat{\mathbf{p}}(s,\mathbf{k}) = \mathcal{L}[\mathring{\mathbf{p}}]$, being $\mathcal{L}$ the bilateral Laplace-transform operator. Pre-multiplying the k-th equation (22) by $\mathbf{T}_k\mathbf{D}_k\mathbf{K}_e$, the $(6+3N)$-by-$(6+3N)$ dynamic stiffness matrix $\mathbf{L}(s,\mathbf{k})$ assumes the convenient quasi-symmetric form

$$\mathbf{L}(s,\mathbf{k}) = \begin{bmatrix}
s^2\,\mathbf{M} + (\mathbf{I}+\mathbf{S})\,\mathbf{K}_e + \mathbf{H}(\mathbf{k}) & -(\mathbf{I}+\mathbf{S})\,\mathbf{K}_e & \ldots & -\mathbf{T}_N\,\mathbf{D}_N\,\mathbf{K}_e \\
-(\mathbf{I}+\mathbf{S})\,\mathbf{K}_e & s^2\,\mathbf{M}_r + (\mathbf{I}+\mathbf{S})\,\mathbf{K}_e & \ldots & \mathbf{T}_N\,\mathbf{D}_N\,\mathbf{K}_e \\
\vdots & \vdots & \ddots & \vdots \\
-\mathbf{T}_N\,\mathbf{D}_N\,\mathbf{K}_e & \mathbf{T}_N\,\mathbf{D}_N\,\mathbf{K}_e & \ldots & (s\,\mathbf{I} + \mathbf{T}_N)\mathbf{T}_N\,\mathbf{D}_N\,\mathbf{K}_e
\end{bmatrix} \tag{27}$$

where it can be recognized that $\mathbf{L}(s,\mathbf{k})$ is not symmetric because $\mathbf{H}(\mathbf{k})$ is Hermitian for the generic wavevector $\mathbf{k}$, but $\mathbf{L}(s,\mathbf{k})$ is not Hermitian because s is complex-valued, in the general case.

4. Triangular beam lattice metamaterial

The general mechanical formulation developed for beam lattice metamaterials is specified hereinafter for the triangular metamaterial univocally characterized by the coordination number $n = 6$, corresponding to a periodic regular hexagonal cell (Fig. 1a,b). The diameter of the circle inscribed in the hexagon coincides with the internodal distance B. Accordingly, the $n/2 = 3$ coordination directions are identified by the unit vectors $\mathbf{n}_1 = [1,0,0]^\top$, $\mathbf{n}_2 = [\cos(\pi/3),\sin(\pi/3),0]^\top$, $\mathbf{n}_3 = [\cos(2\pi/3),\sin(2\pi/3),0]^\top$, respectively, and by the corresponding periodicity vectors $\mathbf{d}_j = B\mathbf{n}_j$ $(j = 1,2,3)$. The physical domain of the regular hexagonal cell can be defined as $\mathcal{D} = \big\{\mathbf{x}\in\mathbb{R}^3 : \big(|x_1| \le B/2\big) \wedge \big(|x_1| \le B + x_2\tan(\pi/3)\big) \wedge \big(|x_1| \le B - x_2\tan(\pi/3)\big) \wedge (x_3 = 0)\big\}$, where symbol $\wedge$ indicates logical conjunction. Accordingly, the geometry of the regular hexagonal domain of the first Brillouin zone of the reciprocal lattice [57], spanned by the wavevector $\mathbf{k} = [k_1,k_2,0]^\top$, is defined as $\mathcal{K} = \big\{\mathbf{k}\in\mathbb{R}^3 : \big(|k_2| \le B_r/2\big) \wedge \big(|k_2| \le B_r + k_1\tan(\pi/3)\big) \wedge \big(|k_2| \le B_r - k_1\tan(\pi/3)\big)\big\}$, where $B_r = 2\pi/(B\sin(\pi/3))$ is the diameter of the circle inscribed in the hexagon (Fig. 1c).

With regard to the dissipation function introduced to model the damping properties the metamaterial, only two terms of the Prony series (i.e., $N = 1$) are considered sufficient to accurately describe the relaxation functions defining the viscoelastic ring-resonator coupling in the triangular beam lattice metamaterial. Therefore, the following expressions are introduced to simplify the notation: $\mathbf{S} = \mathbf{D}_1 \equiv \mathbf{D} = \mathrm{diag}\,(\beta_U,\beta_V,\beta_\phi)$, $\mathbf{T}_1 \equiv \mathbf{T} = t_r^{-1}\mathbf{I}$, and $\mathbf{w}_1(t) \equiv \mathbf{w}(t) = [W_U,W_V,W_\phi]^\top$; therefore, $\mathbf{G}_0 = (\mathbf{I}+\mathbf{D})\,\mathbf{K}_e$.

4.1. Nondimensional form of the equations of motion

The geometric and mechanical parameters of the system can be cast in nondimensional form by introducing suitable characteristic quantities, namely, a circular frequency ω_r and a reference length L_r of the metamaterial, respectively. Hence, the nondimensional time coordinate and Laplace variable become $\tau = \omega_r t$ and $\sigma = s/\omega_r$, respectively, while the displacements of the ring and the resonator can be expressed in nondimensional form as $u = U/L_r$, $v = V/L_r$, and $u_r = U_r/L_r$, $v_r = V_r/L_r$, respectively. On the other hand, the additional viscoelastic states can be nondimensionalized as $w_u = W_U\omega_r/L_r$, $w_v = W_V\omega_r/L_r$, and $w_\phi = W_\phi\omega_r$, respectively; finally, the nondimensional relaxation time is given by $\tau_r = \omega_r t_r$. The nondimensional kinematic descriptors and viscoelastic states can be then collected into the vector of the system variables $\boldsymbol{\varphi}(\tau,\mathbf{b})$ (i.e., the nondimensional counterpart of the vector $\mathbf{q}(t,\mathbf{k})$). Moreover, the nondimensional wave numbers are $\beta_1 = Bk_1$ and $\beta_2 = Bk_2$, respectively, and can be collected in the real-valued wavevector $\mathbf{b} = [\beta_1,\beta_2,0]^\top$, spanning the hexagonal domain of the nondimensional first Brillouin zone represented in Fig. 2a, which can be defined as

$$\mathcal{B} = \big\{\mathbf{b}\in\mathbb{R}^3 : \big(|\beta_2| \le \beta_c\big) \wedge \big(|\beta_2| \le \beta_r + \beta_1\tan\tfrac{\pi}{3}\big) \wedge \big(|\beta_2| \le \beta_r - \beta_1\tan\tfrac{\pi}{3}\big)\big\}\,, \tag{28}$$

where $\beta_r = 2\pi/\sin(\pi/3)$ and $\beta_c = \beta_r/2$ are the nondimensional diameter and radius of the circle inscribed in the hexagon. Finally, the curvilinear abscissa ξ (known also as *reduced wavevector*) is introduced to span the closed triangular boundary of the first irreducible Brillouin zone $\mathcal{B}^*$ identified by the vertices $\mathbf{b}_0$, $\mathbf{b}_1$, $\mathbf{b}_2$ (see Fig. 2a). Accordingly, the components of the nondimensional wavevector $\mathbf{b}$ can be parameterized in terms of ξ as $\beta_1 = \xi$ and $\beta_2 = 0$, for $\xi\in[0,\beta_c\csc(\pi/3)]$, $\beta_1 = \beta_c(\cot(\pi/3)+\csc(\pi/3)) - \xi\cos(\pi/3)$ and $\beta_2 = \xi\sin(\pi/3) - \beta_c$, for $\xi\in[\beta_c\csc(\pi/3),\beta_c(\csc(\pi/3)+\cot(\pi/3))]$, $\beta_1 = \beta_c(\sin(\pi/3)+\cos(\pi/3)+1) - \xi\sin(\pi/3)$ and $\beta_2 = \beta_c(\cot(\pi/3)+\csc(\pi/3)+1)\cos(\pi/3) - \xi\cos(\pi/3)$, for $\xi\in[\beta_c(\csc(\pi/3)+\cot(\pi/3)),\beta_c(1+\csc(\pi/3)+\cot(\pi/3))]$, respectively.

A suited minimal set of nondimensional independent mechanical parameters, sufficient to completely describe the beam lattice metamaterial, is given by the quantities

$$\chi = \frac{R}{L},\quad \chi_r = \frac{R_r}{\sqrt{2}L},\quad \varrho^2 = \frac{M_r}{M},\quad \mu^2 = \frac{J}{AL^2},\quad \kappa_u = \frac{k_U}{\omega_r^2 M},\quad \kappa_v = \frac{k_V}{\omega_r^2 M},\quad \kappa_\phi = \frac{k_\phi}{\omega_r^2 ML^2}, \tag{29}$$

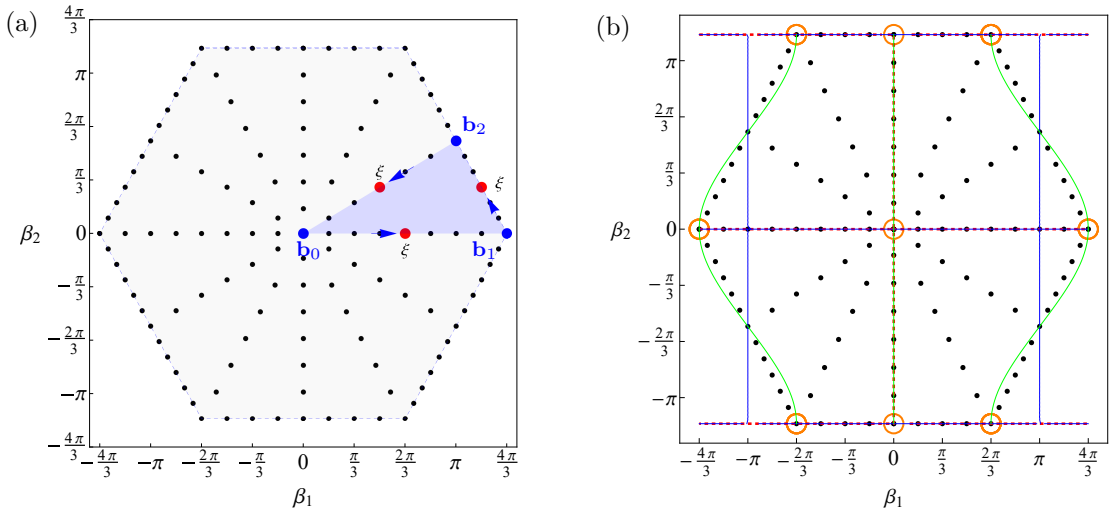

Figure 2: Nondimensional first Brillouin zone $\mathcal{B}$ (gray region) of the triangular beam lattice metamaterial: (a) first irreducible Brillouin zone $\mathcal{B}^*$ (blue region) with vertices $\mathbf{b}_0 = (0,0,0)$, $\mathbf{b}_1 = (\beta_c \csc(\pi/3), 0, 0)$, $\mathbf{b}_2 = (\beta_c \sin(\pi/3), \beta_c \cos(\pi/3), 0)$ (blue dots) and edge midpoints $\mathbf{b}_{01} = (1/2\beta_c \csc(\pi/3), 0, 0)$, $\mathbf{b}_{12} = (\beta_c \sin(\pi/3) + 1/2\beta_c \cos(\pi/3) \cot(\pi/3), 1/2\beta_c \sin(\pi/3) \cot(\pi/3), 0)$, $\mathbf{b}_{20} = (1/2\beta_c \sin(\pi/3), 1/2\beta_c \cos(\pi/3), 0)$, (b) wavevector loci for which the dynamics of the kinematic functions are decoupled.

where the parameter ϱ^2 is the ring-to-resonator mass ratio, while the parameters χ and χ_r account for the rotational-to-translational inertia of the ring and the resonator, respectively. The parameter χ can also be interpreted as a measure of the spatial density of the rings in the metamaterial plane, meaning that – for a fixed ring radius – higher values of χ correspond to a larger number of massive rings per the unit area (say *heavy* metamaterial) and viceversa (say *light* metamaterial), and the nondimensional parameter μ^2 expresses the (inverse of) slenderness of the flexible ligaments. Moreover, the external forces and couples in nondimensional form read $f_u = F_U / \left(\omega_r^2 M L_r\right)$, $f_v = F_V / \left(\omega_r^2 M L_r\right)$, and $f_\phi = F_\phi / \left(\omega_r^2 M L_r^2\right)$, respectively, and are collected in the first three rows of the 9-by-1 vector $\boldsymbol{\delta}(\tau, \mathbf{b})$ representing the nondimensional counterpart of the vector $\mathbf{p}(t, \mathbf{k})$. Finally, the viscoelastic forces and couples can be expressed in nondimensional form as $\gamma_u = g_U / \left(\omega_r^2 M L_r\right)$, $\gamma_v = g_V / \left(\omega_r^2 M L_r\right)$, and $\gamma_\phi = g_\phi / \left(\omega_r^2 M L_r^2\right)$, respectively, and collected in the vector $\boldsymbol{\gamma}(\tau)$, that is, the nondimensional counterpart of the viscoelastic force vector $\mathbf{g}(t)$. Hence, equations of motion (26) can be expressed in nondimensional form as

$$\boldsymbol{\Gamma}(\sigma, \mathbf{b}) \hat{\boldsymbol{\varphi}}(\sigma, \mathbf{b}) = \hat{\boldsymbol{\delta}}(\sigma, \mathbf{b}), \tag{30}$$

where $\hat{\boldsymbol{\varphi}}(\sigma, \mathbf{b})$ and $\hat{\boldsymbol{\delta}}(\sigma, \mathbf{b})$ are the nondimensional vectors of the Laplace transformed counterparts of the $\mathcal{Z}$-transformed variables and forces collected in the vectors $\boldsymbol{\varphi}(\tau, \mathbf{b})$ and $\boldsymbol{\delta}(\tau, \mathbf{b})$, respectively, while the nondimensional 9-by-9 governing matrix $\boldsymbol{\Gamma}(\sigma, \mathbf{b})$ is reported in the Appendix B.

It is worth noting that the internal roto-translational couplings among the three degrees of freedom $\hat{u}$, $\hat{v}$, and $\hat{\phi}$, are provided by the out-of-diagonal σ-independent components of the matrix $\boldsymbol{\Gamma}(\sigma, \mathbf{b})$, which identically vanish (satisfying the condition $\mathcal{C}_{123} : \Gamma_{12}(\mathbf{b}) = \Gamma_{13}(\mathbf{b}) = \Gamma_{23}(\mathbf{b}) = 0$) for the limit of *long wavelengths* $\mathbf{b} = (0, 0, 0)$, located at the center of the hexagonal Brillouin zone, and for the limits of *short wavelengths* $\mathbf{b} = (\pm 4\pi/3, 0, 0)$, $\mathbf{b} = (0, \pm 2\pi/\tan(\pi/3), 0)$, $\mathbf{b} = (2\pi/3, \pm 2\pi/\tan(\pi/3), 0)$, $\mathbf{b} = (-2\pi/3, \pm 2\pi/\tan(\pi/3), 0)$, sitting on the boundary of the hexagon (marked by the orange circles in Fig. 2b). Since all the other submatrices composing the matrix $\boldsymbol{\Gamma}(\sigma, \mathbf{b})$ are diagonal, these $\mathbf{b}$-values correspond to uncoupled equations of free wave propagation and – consequently – perfectly polarized waveforms. Knowing the $\mathbf{b}$ points satisfying the $\mathcal{C}_{123}$-condition may be interesting because perfect or quasi perfect polarization implies that the mechanical

energy propagated by the traveling wave is completely, or nearly completely, stored in a subset of wavecomponents [14]. Furthermore, it can be remarked that other σ-independent wavevector loci realize: (i) perfect uncoupling between the ring translational degrees of freedom $\hat{u}$ and $\hat{v}$ (namely, the $\mathbf{b}$-locus satisfying the condition $\mathcal{C}_{12} : \Gamma_{12}(\mathbf{b}) = 0 = \Gamma_{21}(\mathbf{b})$ and marked by red dashed lines in Fig. 2b); (ii) perfect uncoupling between $\hat{u}$ and $\hat{\phi}$ (condition $\mathcal{C}_{13} : \Gamma_{13}(\mathbf{b}) = 0 = -\Gamma_{31}(\mathbf{b})$, blue solid lines) and between $\hat{v}$ and $\hat{\phi}$ (condition $\mathcal{C}_{23} : \Gamma_{23}(\mathbf{b}) = 0 = -\Gamma_{32}(\mathbf{b})$, green solid lines). In particular, it is interesting to note that the whole subdomain $\beta_2 = 0$ is characterized by uncoupled dynamics of the translational degrees of freedom $\hat{u}$ and $\hat{v}$ and the rototranslational degrees of freedom $\hat{u}$ and $\hat{\phi}$.

In the next Sections, equations (30) are analyzed to describe the free and forced propagation of harmonic waves. For illustrative purposes, a particular metamaterial $\mathcal{M}$ is selected as reference, by fixing the values of the mechanical parameters in technically feasible ranges. Specifically, the nondimensional geometrical, inertial and elastic parameters are $\varrho^2 = 25/6$, $\chi^2 = 1/25$, $\chi_r^2 = 1/200$, $\mu^2 = 1/4800$ (consistently with [56]). The nondimensional viscoelastic parameters of the metamaterial $\mathcal{M}$ are $\tau_r = 1/5$, $\kappa_u = \kappa_v = 7/20$, $\kappa_\phi = 4/625$, and $\beta_U = \beta_V = \beta_\phi = 1$. Moreover, the stiffer undamped metamaterial $\mathcal{M}_\infty$ (for $\tau_r \to +\infty$) and softer undamped metamaterial $\mathcal{M}_0$ (for $\tau_r \to 0^+$) are considered as limit conditions.

5. Free wave propagation

The free damped oscillations of the triangular beam lattice metamaterial are conveniently studied in the frequency domain. By neglecting the external excitation, hence setting $\hat{\boldsymbol{\delta}}(\sigma, \mathbf{b}) = \mathbf{0}$ in Eq. (30), the $\mathbf{b}$-dependent system of homogeneous algebraic equations governing the free wave propagation can be recognized as a non-standard eigenproblem in the form

$$\boldsymbol{\Gamma}(\sigma, \mathbf{b})\hat{\boldsymbol{\varphi}}(\sigma, \mathbf{b}) = \mathbf{0}, \tag{31}$$

whose non-trivial solution, that can be calculated by imposing the characteristic equation $\det \boldsymbol{\Gamma}(\sigma, \mathbf{b}) = 0$, delivers fifteenth eigenpairs $(\sigma, \hat{\boldsymbol{\varphi}})$ for each selected wavevector $\mathbf{b}$. Among them, six pairs of complex-conjugate and three real negative eigenvalues can be distinguished, corresponding to six complex-conjugate and three complex eigenvectors $\hat{\boldsymbol{\varphi}}$, respectively. In particular, the eigenvectors associated with the three real eigenvalues σ turn out to be real-valued vectors only if the rotational and the translational degrees of freedom are uncoupled (that is, when $\Gamma_{13} = \Gamma_{23} = 0$). From the mechanical point of view, σ and $\hat{\boldsymbol{\varphi}}$ play the role of complex-valued wavefrequency and waveform, respectively, for the Bloch wave propagating according to the real-valued wavevector $\mathbf{b}$. Complex-conjugate wavefrequencies are related to couples of forward and backward waves propagating with $\mathcal{I}(\sigma)$-monoharmonic oscillations and exponentially time-decaying amplitude whose rate is proportional to $\mathcal{R}(\sigma)$, associated to a damping ratio $\zeta = -\mathcal{R}(\sigma)/|\sigma|$

Table 1: Wavefrequencies of the triangular beam lattice metamaterial at notable wavevector values of the first irreducible Brillouin zone $\mathcal{B}^*$.

	$\mathbf{b}_0$ $(0,0,0)$	$\mathbf{b}_{01}$ $(\frac{2}{3}\pi,0,0)$	$\mathbf{b}_1$ $(\frac{4}{3}\pi,0,0)$	$\mathbf{b}_{12}$ $(\frac{7}{6}\pi,\frac{1}{2\sqrt{3}}\pi,0)$	$\mathbf{b}_2$ $(\pi,\frac{1}{\sqrt{3}}\pi,0)$	$\mathbf{b}_{20}$ $(\frac{1}{2}\pi,\frac{1}{2\sqrt{3}}\pi,0)$
σ_1	0	-0.005+0.26$\imath$	-0.007+0.279$\imath$	-0.007+0.274$\imath$	-0.006+0.267$\imath$	-0.004+0.248$\imath$
σ_2	0	-0.007+0.276$\imath$	-0.007+0.279$\imath$	-0.007+0.281$\imath$	-0.007+0.282$\imath$	-0.007+0.274$\imath$
σ_3	-0.007+0.413$\imath$	-0.003+0.357$\imath$	-0.001+0.285$\imath$	-0.001+0.297$\imath$	-0.001+0.306$\imath$	-0.004+0.37$\imath$
σ_4	-0.043+0.663$\imath$	-0.043+0.767$\imath$	-0.046+0.729$\imath$	-0.045+0.734$\imath$	-0.045+0.738$\imath$	-0.043+0.777$\imath$
σ_5	-0.043+0.663$\imath$	-0.036+1.379$\imath$	-0.031+2.219$\imath$	-0.033+1.811$\imath$	-0.035+1.552$\imath$	-0.038+1.183$\imath$
σ_6	-0.04+0.82$\imath$	-0.032+1.977$\imath$	-0.031+2.219$\imath$	-0.029+2.455$\imath$	-0.029+2.536$\imath$	-0.033+1.845$\imath$
σ_7	-4.913	-4.922	-4.924	-4.926	-4.927	-4.921
σ_8	-4.913	-4.917	-4.924	-4.921	-4.919	-4.916
σ_9	-4.907	-4.907	-4.907	-4.907	-4.907	-4.907

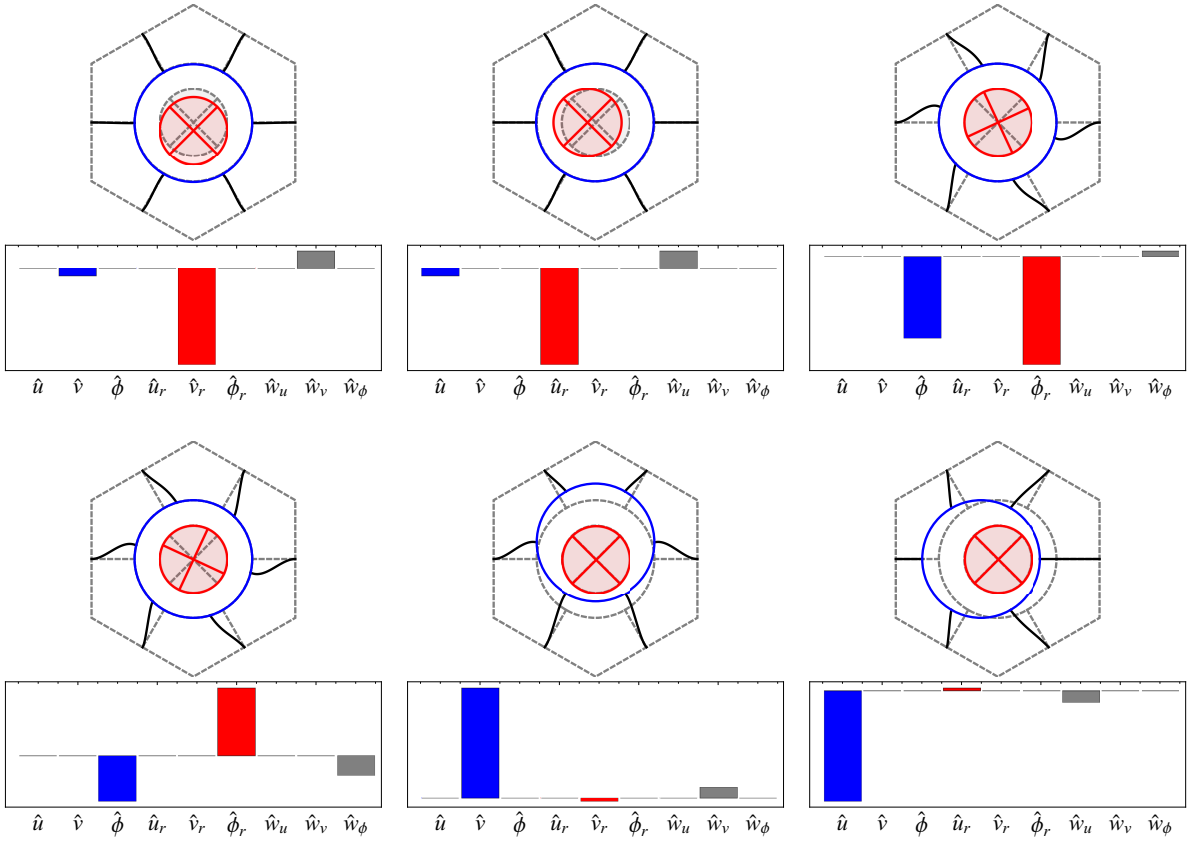

Figure 3: Real form of the waveforms and wavecomponents of the triangular beam lattice metamaterial at the limit of short wavelength $\mathbf{b}_1$: waveforms $\hat{\boldsymbol{\varphi}}_1$, $\hat{\boldsymbol{\varphi}}_2$, $\hat{\boldsymbol{\varphi}}_3$ (top, from left to right), and $\hat{\boldsymbol{\varphi}}_4$, $\hat{\boldsymbol{\varphi}}_5$, $\hat{\boldsymbol{\varphi}}_6$ (bottom, from left to right).

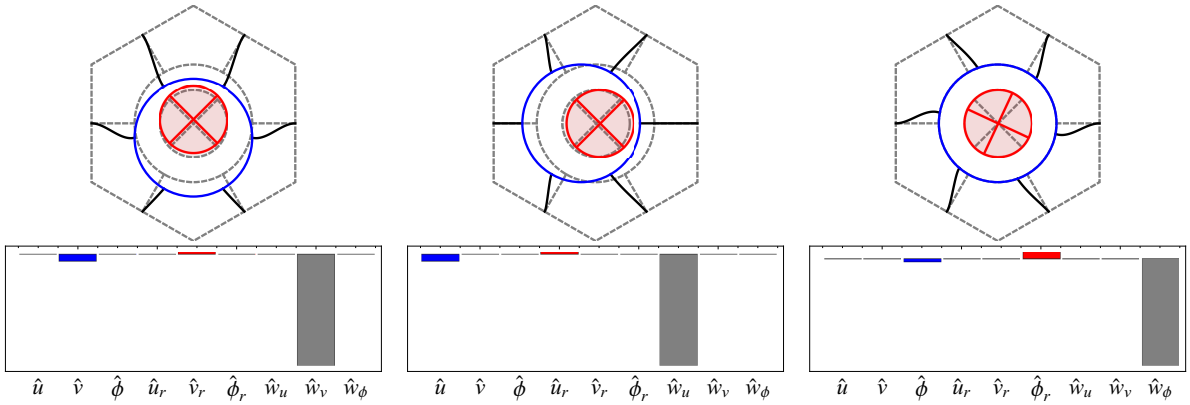

Figure 4: Real form of the waveforms and wavecomponents of the triangular beam lattice metamaterial at the limit of short wavelength $\mathbf{b}_1$: waveforms $\hat{\boldsymbol{\varphi}}_7$, $\hat{\boldsymbol{\varphi}}_8$, $\hat{\boldsymbol{\varphi}}_9$ (from left to right).

(normalized with respect the critical damping attained for $\zeta_{cr} = 1$), where $|\sigma|$ stands for the magnitude of the complex wavefrequency σ. On the other hand, negative real-valued wavefrequencies are related to standing (non propagating) waves with exponentially time-decaying amplitude. It may be worth noting that the mechanical formulation based on the added viscoelastic states has the methodological advantage of stating a polynomial eigenproblem, thus bypassing the algorithmic complexities of de-rationalizing or asymptotically approximating the characteristic polynomial [56].

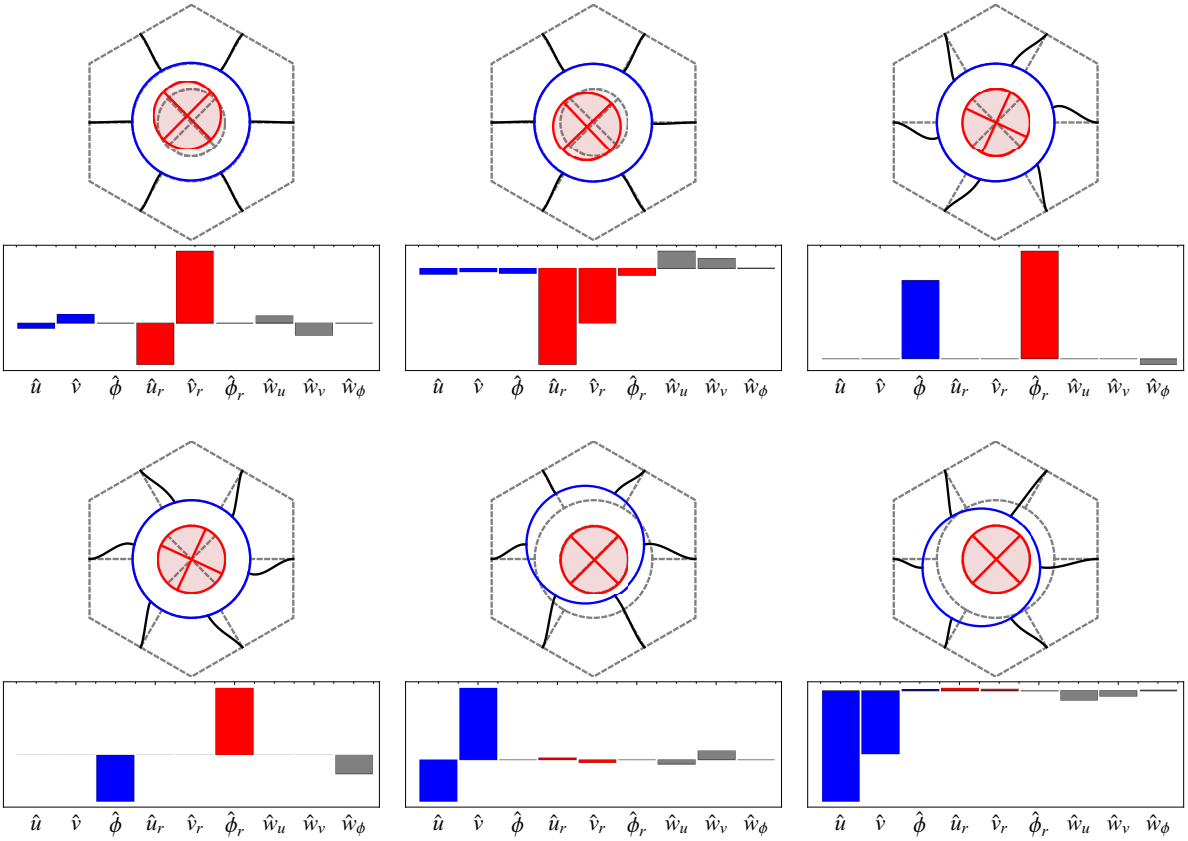

Figure 5: Real form of the waveforms and wavecomponents of the triangular beam lattice metamaterial at the wavevector $\mathbf{b}_{12}$: waveforms $\hat{\boldsymbol{\varphi}}_1$, $\hat{\boldsymbol{\varphi}}_2$, $\hat{\boldsymbol{\varphi}}_3$ (top, from left to right), and $\hat{\boldsymbol{\varphi}}_4$, $\hat{\boldsymbol{\varphi}}_5$, $\hat{\boldsymbol{\varphi}}_6$ (bottom, from left to right).

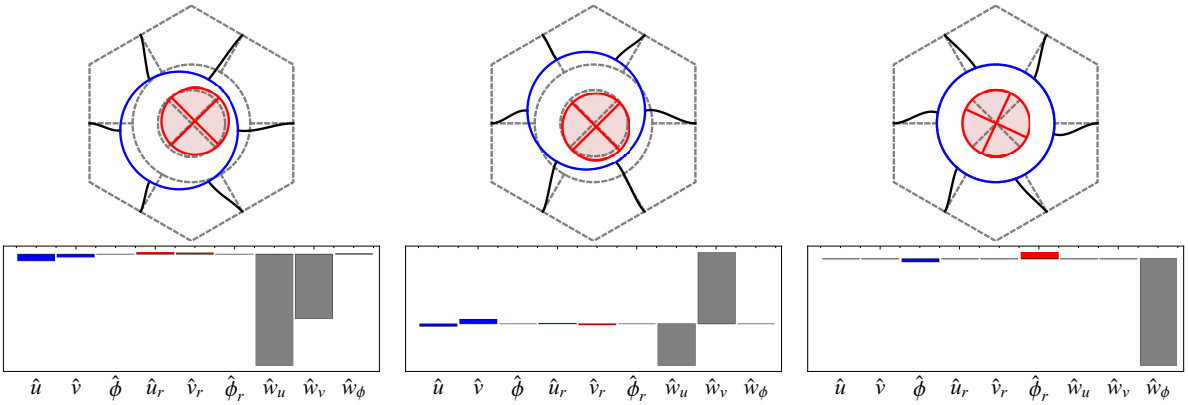

Figure 6: Real form of the waveforms and wavecomponents of the triangular beam lattice metamaterial at the wavevector $\mathbf{b}_{12}$: waveforms $\hat{\boldsymbol{\varphi}}_7$, $\hat{\boldsymbol{\varphi}}_8$, $\hat{\boldsymbol{\varphi}}_9$ (from left to right).

The eigenvalues σ corresponding to notable wavevector $\mathbf{b}$-values in the first irreducible Brillouin zone $\mathcal{B}^*$ (namely the vertices $\mathbf{b}_0$, $\mathbf{b}_1$, $\mathbf{b}_2$ and the midpoints $\mathbf{b}_{01}$, $\mathbf{b}_{12}$, $\mathbf{b}_{20}$ of each edge, marked by blue and red dots in Fig. 2a, respectively) are reported in Tab. 1. Complex conjugate wavefrequencies corresponding to backward waves (with negative imaginary part) are not reported for the sake of synthesis. It is worth noting that the six complex wavefrequencies σ_1-σ_6 (as well as their conjugates) are systematically characterized by a real parts significantly smaller than those of the three real-valued wavefrequencies σ_7-σ_9. This characteristic scenario

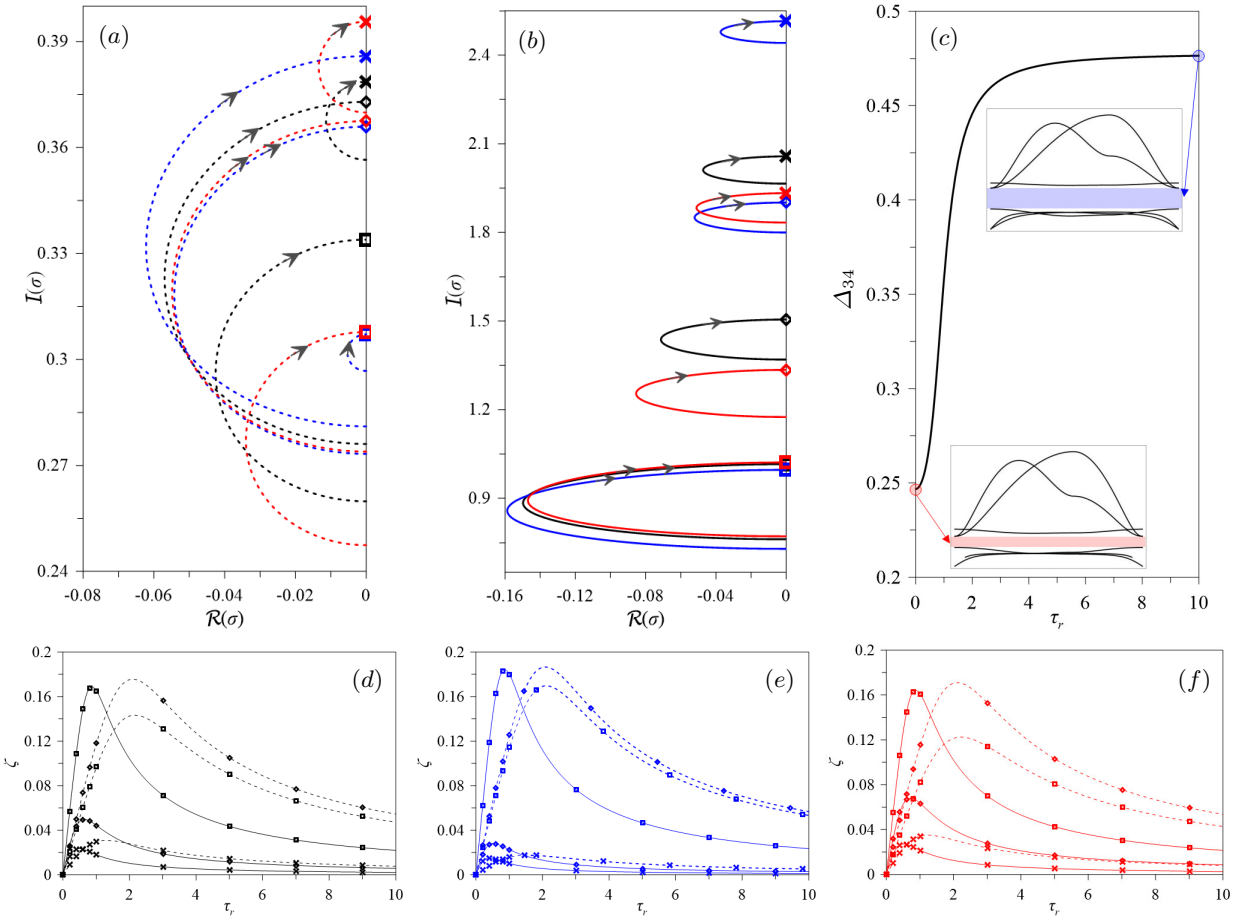

Figure 7: Loci of complex-valued frequencies σ under variation of the relaxation time (gray arrows indicate increasing relaxation time in the range $\tau_r \in [10^{-3}, 10^3]$) for wavevectors $\mathbf{b}_{01}$ (black lines), $\mathbf{b}_{12}$ (blue lines), $\mathbf{b}_{20}$ (red lines): (a) frequencies from the low-frequency spectral branches (dashed lines) and (b) frequencies from the high-frequency spectral branches (solid lines); (c) amplitude of the stop bandwidth between the low and high-frequency spectral branches, with spectra for $\tau_r = 0$ (red stop band) and $\tau_r = 10$ (blue stop band); (d), (e), (f) damping ratios ζ under variation of the relaxation time in the range $\tau_r \in [10^{-3}, 10]$.

is physically justified by the typical waveforms associated with the wavefrequencies. Indeed, the waveforms $\hat{\boldsymbol{\varphi}}_1$-$\hat{\boldsymbol{\varphi}}_6$ associated to the complex conjugate wavefrequencies σ_1-σ_6 mainly involve the ring and resonator dynamics, with more or less polarization in one or the other wavecomponents, but minimal participation of the added viscoelastic states. Conversely, the waveforms $\hat{\boldsymbol{\varphi}}_7$-$\hat{\boldsymbol{\varphi}}_9$ associated to the real wavefrequencies σ_7-σ_9 are strongly polarized in the added viscoelastic states, with minimal participation of the ring and resonator. To exemplify, the real forms of the waveforms corresponding to the limit of short wavelength $\mathbf{b}_1$, satisfying the full uncoupling condition $\mathcal{C}_{123}$, are depicted in Fig. 3 and Fig. 4. As expected, the waveforms $\hat{\boldsymbol{\varphi}}_1$ and $\hat{\boldsymbol{\varphi}}_5$ are dominated by the ring and resonator dynamics, with strong polarization in the wavecomponent subset $(\hat{v}, \hat{v}_r)$ and minimal participation of the added viscoelastic states (Fig. 3). Similar results are appreciable for the waveforms $\hat{\boldsymbol{\varphi}}_2$ and $\hat{\boldsymbol{\varphi}}_6$, strongly polarized in the wavecomponent subset $(\hat{u}, \hat{u}_r)$, and $\hat{\boldsymbol{\varphi}}_3$ and $\hat{\boldsymbol{\varphi}}_4$, strongly polarized in the wavecomponent subset $(\hat{\phi}, \hat{\phi}_r)$. Conversely, the waveforms $\hat{\boldsymbol{\varphi}}_7$-$\hat{\boldsymbol{\varphi}}_9$ are strongly polarized in the added viscoelastic states $\hat{w}_u$, $\hat{w}_v$ and $\hat{w}_\phi$, respectively (Fig. 4). The waveforms corresponding to the wavevector $\mathbf{b}_{12}$, providing instead full internal coupling (that is $\mathcal{C}_{12}$, $\mathcal{C}_{23}$, $\mathcal{C}_{13}$ not satisfied), are shown in Fig. 5 and Fig. 6. As expected, the waveforms $\hat{\boldsymbol{\varphi}}_1$-$\hat{\boldsymbol{\varphi}}_6$ are participated in a comparable manner by all the wavecomponents of the ring and the resonator (Fig. 5), whereas the waveforms $\hat{\boldsymbol{\varphi}}_7$-$\hat{\boldsymbol{\varphi}}_9$ remain strongly polarized in the added viscoelastic states (Fig. 6).

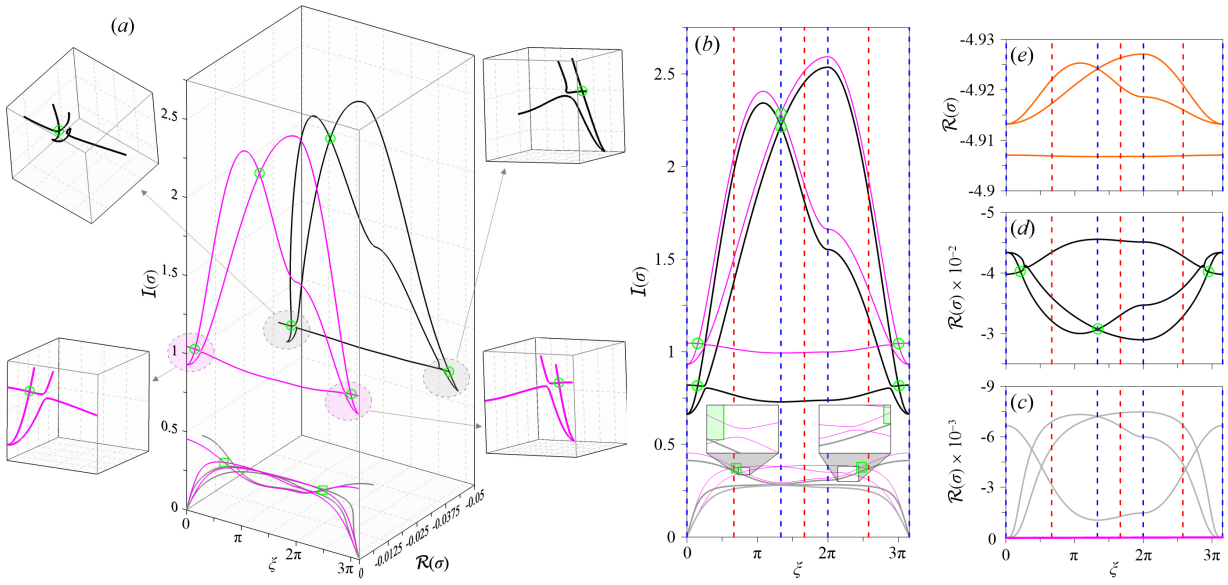

Figure 8: Frequency dispersion spectrum of the undamped metamaterial $\mathcal{M}_\infty$ (magenta curves) and the damped metamaterial $\mathcal{M}$ (gray, black and orange curves): (a) spectra in the three-dimensional domain $(\xi, \mathcal{I}(\sigma), \mathcal{R}(\sigma))$, (b) spectra in the two-dimensional domain $(\xi, \mathcal{I}(\sigma))$, (c),(d),(e) spectra in the two-dimensional domain $(\xi, \mathcal{R}(\sigma))$. Dashed-blue and dashed red vertical lines indicate reduced wavevectors ξ corresponding to $\mathbf{b}_0$, $\mathbf{b}_1$, $\mathbf{b}_2$ and $\mathbf{b}_{01}$, $\mathbf{b}_{12}$, $\mathbf{b}_{20}$, respectively.

A comprehensive analysis of the spectral effects provided by the dissipative ring-resonator coupling may require a suited parametric analysis focused on the relaxation time, which is the key parameter governing the assumed viscoelastic law. The loci of the complex-valued frequencies σ of the metamaterial $\mathcal{M}$ are illustrated in Figs. 7a,b under large variation of the relaxation time τ_r for selected wavevectors $\mathbf{b}$ corresponding to the red points in Fig. 2a. From the quantitative viewpoint, it is worth noting that the three complex frequencies σ having lower imaginary part are associated with lower real parts (Fig. 7a), whereas the three complex frequencies σ having higher imaginary part are associated with larger real parts (Fig. 7b). From the qualitative viewpoint, it can be observed that the real part $\mathcal{R}(\sigma)$ strictly depends on the relaxation time τ_r and – as major remark – it always shows a minimum between the limit conditions of softer undamped metamaterial $\mathcal{M}_0$ (for $\tau_r \to 0^+$) and the stiffer undamped metamaterial $\mathcal{M}_\infty$ (for $\tau_r \to +\infty$). From a physical perspective, this relevant remark highlights how the damping ratio ζ of the spectral branches does not monotonically grow with the viscosity increments of the ring-resonator coupling regulated by decrements of the relaxation time τ_r. Consequently, particular relaxation times providing the maximal decay rate in the amplitude of damped propagating waves can be identified. This peculiar scenario is also known to characterize a variety of viscoelastically-coupled engineering structures, and has been often exploited to develop optimization strategies for passive control [58, 59]. To investigate the phenomenon, the behavior of the damping ratio ζ versus the relaxation time τ_r is analyzed numerically and illustrated in Figs. 7d-f for different wavevectors. The results show that damping maxima exist for all the spectral branches, although they may significantly differ in magnitude. Damping maxima also are attained at lower relaxation times ($\tau_r \approx 1$) for high-frequency branches (solid lines), and at larger relaxation times ($\tau_r \approx 2$) for low-frequency branches (dashed lines). Within this context, the relaxation time characterizing the ring-resonator coupling of the reference metamaterial $\mathcal{M}$ (namely $\tau_r = 1/5$) is selected so as to provide large damping of the high-frequency waves and low damping of the low-frequency waves. As complementary remark, a direct comparison among Figs. 7d-f evidences how the relaxation time corresponding to the maximum damping ratio of each spectral branch does not depend significantly on the wavevector $\mathbf{b}$.

The dispersion spectrum $\sigma(\mathbf{b})$ of the damped metamaterial $\mathcal{M}$ is fully defined by spanning the first irreducible Brillouin zone $\mathcal{B}^*$ with the wavevector $\mathbf{b}$. A comprehensive but synthetic description of the spectrum can be obtained in the form $\sigma(\xi)$, by spanning the closed boundary $\partial\mathcal{B}^*$ of $\mathcal{B}^*$ (see Fig. 2a) with the reduced wavevector ξ. The representation of the spectrum in the three-dimensional domain $(\xi, \mathcal{I}(\sigma), \mathcal{R}(\sigma))$ is shown in Fig. 8a, where only the complex eigenvalues σ having positive imaginary part are reported and

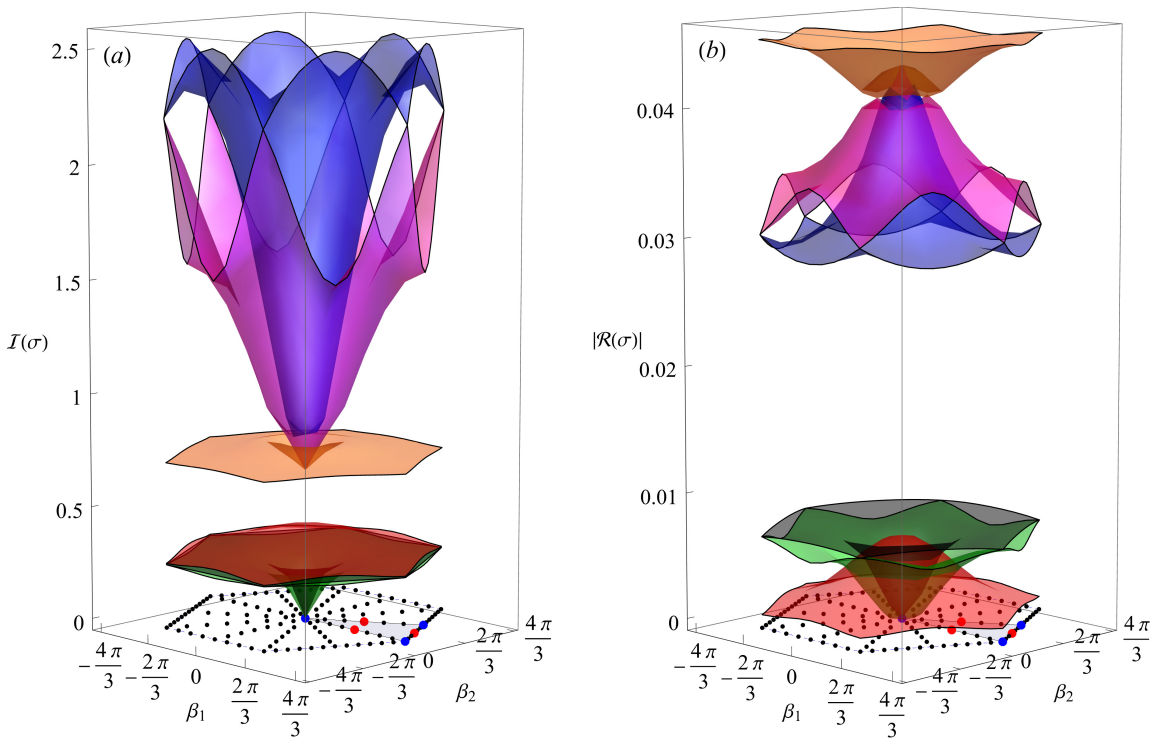

Figure 9: Dispersion spectra of the damped metamaterial $\mathcal{M}$: (a) imaginary part and (b) real part of the complex-valued dispersion surfaces over the whole first Brillouin zone $\mathcal{B}$.

the case of *stiffer* undamped metamaterial $\mathcal{M}_\infty$ (magenta lines) and damped metamaterial $\mathcal{M}$ (black and gray lines) are compared. The undamped metamaterial $\mathcal{M}_\infty$ shows a dispersion spectrum composed by six branches. All the spectral branches are purely imaginary and systematically lie in the plane $(\xi, \mathcal{I}(\sigma))$. The typical scenario of three low-frequency dispersion curves (with waveforms strongly polarized in the ring wavecomponents) and three high-frequency dispersion curves (with waveforms strongly polarized in the resonator wavecomponents), separated by a frequency band gap, can be recognized. Differently, the damped metamaterial $\mathcal{M}$ shows a dispersion spectrum composed by nine branches. Three curves lie in the low-frequency range (*low-frequency curves* marked by gray lines in Figs. 8a,b) and can be considered as spectral branches of weak-attenuation, since they are associated with lower real parts (low damping ratios), as shown in Fig. 8c. Three curves lie in the high-frequency range (*high-frequency curves* marked by black lines in Figs. 8a,b) and can be considered spectral branches of strong-attenuation since they are associated with higher real parts (high damping ratios), as shown in Fig. 8d. It is interesting to note that the viscoelastic coupling produces a strong frequency reduction of the three high-frequency curves and a remarkable decrease of the low-frequency curves over a wide ξ-range (Fig. 8b). This implies a not negligible decrement in the stop bandwidth, that is, the gap between the imaginary parts of the high-frequency and the low-frequency curves, together with a small shift of the stop band centerfrequency. The dependence of the stop bandwidth on increasing relaxation times is analyzed in Fig. 7c, where the bandwith $\Delta_{34} = \min_{\partial\mathcal{B}^*}(\mathcal{I}(\sigma_4)) - \max_{\partial\mathcal{B}^*}(\mathcal{I}(\sigma_3))$ can be observed to increase monotonically from $\tau_r = 0$ and to tend to an asymptotic value for large τ_r (say greater than $\tau_r = 10$). In particular, the stop bandwidth attains the value $\Delta_{34} \simeq 0.25$ for the relaxation time $\tau_r = 1/5$ of the metamaterial $\mathcal{M}$. The real-valued eigenvalues corresponding to waveforms polarized in the added viscoelastic states determine the last three dispersion curves lying in the highly-negative $\mathcal{R}(\sigma)$-range of the $(\xi, \mathcal{R}(\sigma))$-plane (high-damping curves, marked by orange lines in Fig. 8e) and can be considered as spectral branches of pure-attenuation corresponding to non-periodic highly overdamped waves.

Focusing on the intersection between two spectral branches, referred to as *cross-overs* or *crossing* points, it is interesting to highlight that the two cross-overs involving the imaginary-valued high-frequency branches of

the undamped metamaterial $\mathcal{M}_\infty$ are preserved in the complex-valued spectrum of the damped metamaterial $\mathcal{M}$ (crossing points marked by green circles of the magenta and black dispersion curves at wavevectors close to the limit of long wavelengths $\mathbf{b} = \mathbf{0}$). The same behaviour is shown also by the cross-over occurring at the wavevector $\mathbf{b}_1$. On the contrary, the two cross-overs involving the low-frequency branches of the undamped metamaterial $\mathcal{M}_\infty$ disappear in the spectrum of the damped metamaterial $\mathcal{M}$ (crossing points marked by green squares of the magenta dispersion curves at wavevectors $\mathbf{b} \simeq \mathbf{b}_{01}$ and $\mathbf{b} \simeq \mathbf{b}_{20}$). Attention can also be paid to the *veering* (avoided crossing) points, in which strong linear interactions and energy transfers may occur between the waveforms [14]. Two relevant veering points can be detected in the high-frequency branches of the undamped metamaterial $\mathcal{M}_\infty$ (within the magenta regions in Fig. 8a and windows in Fig. 8b). These *veering* points are found to persist also in the complex-valued spectrum of the damped metamaterial $\mathcal{M}$.

Finally, the six complex-valued dispersion surfaces of the frequency spectrum for the damped metamaterial $\mathcal{M}$ are illustrated over the whole first Brillouin zone $\mathcal{B}$ in Fig. 9. Looking first at the imaginary part of the dispersion surfaces, the large amplitude of the full band gap separating the low-frequency pass band and the high-frequency pass band can be appreciated (Fig. 9a). Furthermore, coalescence of the two highest and the two lowest dispersion surfaces can be noted to occur at all the six vertices of the hexagonal Brillouin zone $\mathcal{B}$. In these points, the geometrical topology of the coalescent dispersion surfaces resembles the typical Dirac cones characterizing the electronic band structure of monolayer graphene sheets, similarly featured by a periodic hexagonal cell [60]. Looking at the real part of the dispersion surfaces, the large differences characterizing the low-frequency and high-frequency dispersion surfaces can be appreciated (Fig. 9b).

6. Forced wave propagation

The forced response of the damped mechanical metamaterial can be studied either in the frequency or in the time domain. In the frequency domain, the solution of the equations of motion, in nondimensional form, can be determined by inverting the dynamic stiffness matrix $\mathbf{\Gamma}(\sigma, \mathbf{b})$ in Eq. (30) so as to obtain

$$\hat{\boldsymbol{\varphi}}(\sigma, \mathbf{b}) = \mathbf{\Gamma}(\sigma, \mathbf{b})^{-1} \hat{\boldsymbol{\delta}}(\sigma, \mathbf{b}) \tag{32}$$

where $\mathbf{\Gamma}(\sigma, \mathbf{b})^{-1}$ can be regarded as dynamic compliance (or flexibility) matrix. By then applying, first, the inverse bilateral Laplace transform and, second, the inverse discrete Fourier transform (see [56] for details) it is possible to calculate the dynamic response in the time domain and physical space.

Alternately, the forced response can be determined by solving analytically (according to the procedure detailed in Appendix C) or by integrating numerically the ordinary differential equations of motion expressed in the time domain and in the reciprocal space. Specifically, equations (24) can be particularized for the triangular beam lattice metamaterial and expressed in nondimensional form as

$$\mathbf{\Pi}(\mathring{\boldsymbol{\varphi}}(\tau, \mathbf{b}))^{\cdot\cdot} + \mathbf{\Upsilon}(\mathring{\boldsymbol{\varphi}}(\tau, \mathbf{b}))^{\cdot} + \mathbf{\Sigma}(\mathbf{b})\, \mathring{\boldsymbol{\varphi}}(\tau, \mathbf{b}) = \mathring{\boldsymbol{\delta}}(\tau, \mathbf{b}), \tag{33}$$

where the nondimensional 9-by-9 mass matrix $\mathbf{\Pi} = \mathrm{diag}(\mathbf{\Pi}_a, \mathbf{\Pi}_r, \mathbf{O})$ with $\mathbf{\Pi}_a = \mathrm{diag}\,(1, 1, \chi^2)$ and $\mathbf{\Pi}_r = \mathrm{diag}\,(\varrho^2, \varrho^2, \chi_r^2)$, the nondimensional 9-by-9 matrix $\mathbf{\Upsilon} = \mathrm{diag}(\mathbf{O}, \mathbf{O}, \mathbf{I})$ and the nondimensional 9-by-9 generalized stiffness matrix $\mathbf{\Sigma}(\mathbf{b})$ is not-symmetric, $\mathbf{b}$-dependent and reported in the Appendix B. Once the solution $\boldsymbol{\varphi}(\tau, \mathbf{b})$ is analytically or numerically known in the reciprocal space, the forced response $\boldsymbol{\varphi}_{\mathcal{J}}(\tau)$ in the physical space can be determined by applying the inverse discrete Fourier transform

$$\boldsymbol{\varphi}_{\mathcal{J}}(\tau) = \mathcal{F}_d^{-1}[\mathring{\boldsymbol{\varphi}}(\tau, \mathbf{k})] = \frac{1}{|\mathcal{B}|} \int_{\mathcal{B}} \mathring{\boldsymbol{\varphi}}(\tau, \mathbf{b}) \exp[\imath(i_1 - 1)(\mathbf{n}_1 \cdot \mathbf{b})] \ldots \exp[\imath(i_{n/2} - 1)(\mathbf{n}_{n/2} \cdot \mathbf{b})] \mathrm{d}\mathbf{b}, \tag{34}$$

where $|\mathcal{B}|$ is the size of the first Brillouin zone.

By virtue of the dynamic problem linearity and without loss of generality, it may be convenient to analyze the forced response to a single punctual excitation $\boldsymbol{\delta}_{\mathcal{J}}(\tau)$ applied to the $\mathcal{J}$-th lattice node, taken as reference for the sake of simplicity (namely $\mathcal{J} = \mathcal{O}$). Specifically, the generic real-valued mono-harmonic component

$$\boldsymbol{\delta}_{\mathcal{O}}(\tau) = \boldsymbol{\delta}_{(0,\ldots,0)}(\tau) = \tfrac{1}{2} \boldsymbol{\psi} H(\tau) \exp(\varsigma\, \tau) + cc, \tag{35}$$

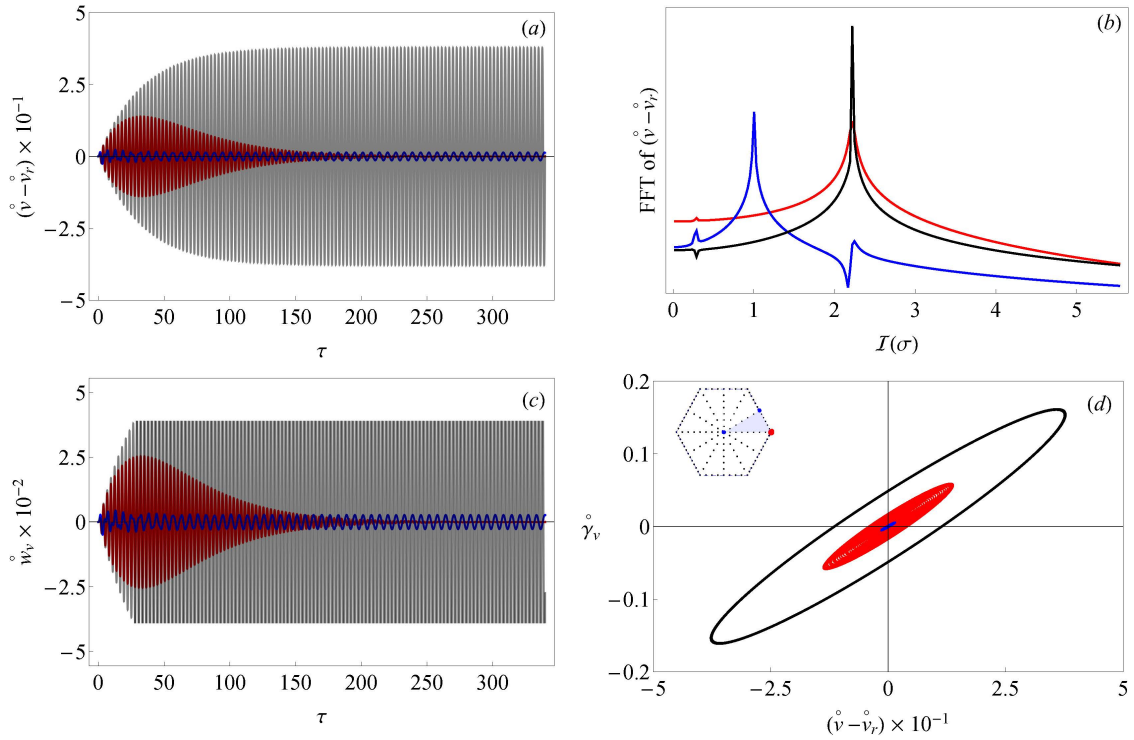

Figure 10: Forced response to harmonic punctual force characterized by monocomponent amplitude vector $\boldsymbol{\psi}_v$ (not-null component $\psi_v = 5\times10^{-2}$) for wavevector $\mathbf{b}_1$ in the resonant (red lines), quasi-resonant (black lines) and non-resonant (blue lines) cases: (*a*), (*b*) time history and FFT of the relative displacement $(\mathring{v}-\mathring{v}_r)$; (*c*) time history of the viscoelastic state $\mathring{w}_v$; (*d*) oscillation cycles of viscoelastic force $\mathring{\gamma}_v$ versus relative displacement $(\mathring{v}-\mathring{v}_r)$.

of a time-periodic force is considered, with constant amplitude 9-by-1 vector $\boldsymbol{\psi} = [\psi_u, \psi_v, \psi_\phi, 0, ..., 0]^\top$, complex nondimensional excitation frequency ς, $H(\tau)$ indicating the unit step function and *cc* standing for complex conjugate. In particular, the analyses in the following are limited to non-decaying ($\mathcal{R}(\varsigma) = 0$) or exponentially decaying ($\mathcal{R}(\varsigma) < 0$) excitations. Under these assumptions, the mapped $\mathcal{Z}$-transform of the excitation is $\mathbf{b}$-independent and reads $\mathring{\boldsymbol{\delta}}(\tau) = \frac{1}{2}\boldsymbol{\psi}H(\tau)\exp(\varsigma\,\tau) + cc$.

Hereinafter, the forced responses $\mathring{\boldsymbol{\varphi}}(\tau, \mathbf{b})$ are investigated separately for punctual forces ψ_u, ψ_v or punctual couples ψ_ϕ and different values of the wavevector $\mathbf{b}$, particularizing the stiffness matrix $\boldsymbol{\Sigma}(\mathbf{b})$, by direct time integrations of Eq. (33). Moreover, the added-state formulation, which by-passes the computational issues related to the presence of convolution integrals in the equations of motion, is exploited to directly assess in time the dynamics of the viscoelastic states. This implies also the valuable possibility of evaluating, straightforwardly, the dissipative force vector $\mathring{\boldsymbol{\gamma}}(\tau)$ (i.e., the mapped $\mathcal{Z}$-transform of the nondimensional vector $\boldsymbol{\gamma}(\tau)$) through the expression given in Eq. (15). Consequently, the force-displacement cycles can be obtained and employed to determine the energy dissipated by the viscoelastic resonators.

The forced response to a particular harmonic punctual force characterized by monocomponent amplitude vector $\boldsymbol{\psi}_v$ (where $\psi_v = 5\times10^{-2}$, while $\psi_u = \psi_\phi = 0$) and different excitation frequencies is illustrated in Fig. 10 for the stiffness matrix particularized by fixed wavevector $\mathbf{b}_1$. Specifically, the time-histories of the real-valued relative ring-resonator displacement $(\mathring{v}-\mathring{v}_r)$ and the corresponding viscoelastic state $\mathring{w}_v$ are illustrated in Figs. 10a,c. For the relative displacement, the fast Fourier transform (FFT) is shown in Fig. 10b. Finally, the oscillation cycles of the viscoelastic force $\mathring{\gamma}_v$ versus the relative displacement $(\mathring{v}-\mathring{v}_r)$ are portrayed in Fig. 10d. Since the wavevector $\mathbf{b}_1$ satisfies the condition of full decoupling $\mathcal{C}_{123}$, the forced response involves only the waveforms $\boldsymbol{\varphi}_1$ and $\boldsymbol{\varphi}_5$ participated by the wavecomponents $\mathring{v}$ and $\mathring{v}_r$ (*activable* waveforms). Three cases of interest are analyzed: (i) the *resonant* case of time-decaying force having real and imaginary parts of the excitation frequency equal to a certain harmonic component of the spectrum

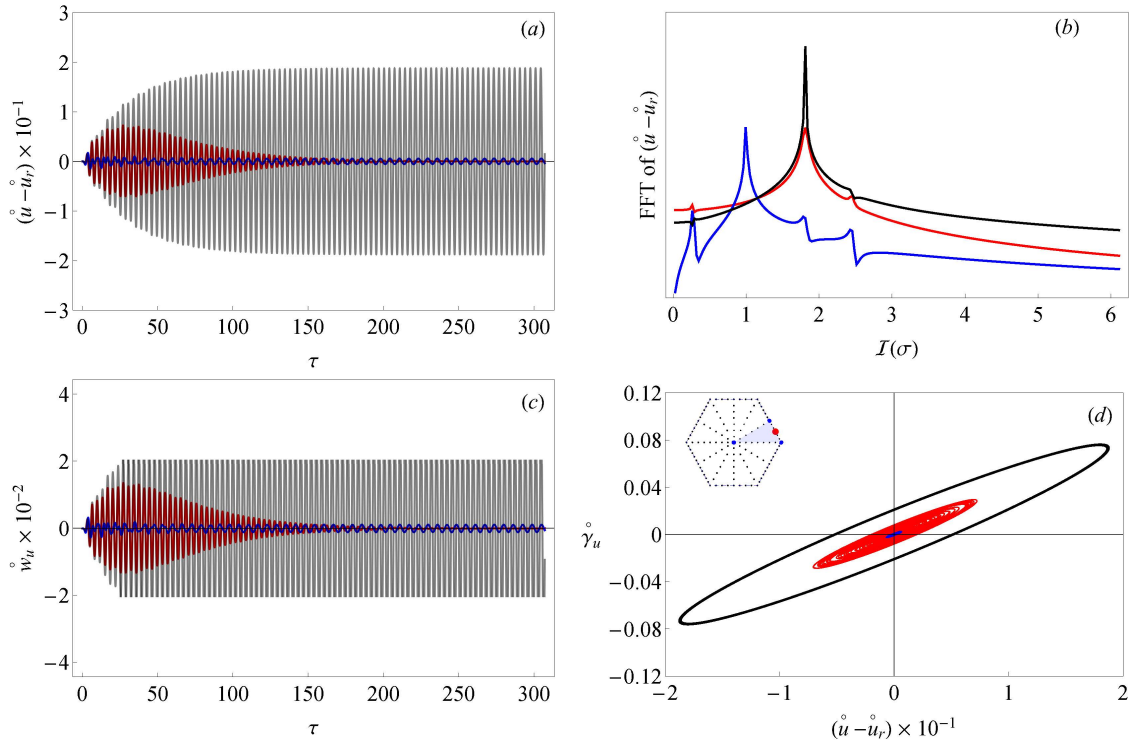

Figure 11: Forced response to harmonic punctual force characterized by monocomponent amplitude vector $\boldsymbol{\psi}_v$ (not-null component $\psi_v = 5 \times 10^{-2}$) for wavevector $\mathbf{b}_{12}$ in the resonant (red lines), quasi-resonant (black lines) and non-resonant (blue lines) cases: (*a*), (*b*) time history and FFT of the relative displacement $(\mathring{u} - \mathring{u}_r)$; (*c*) time history of the viscoelastic state $\mathring{w}_u$; (*d*) oscillation cycles of viscoelastic force $\mathring{\gamma}_u$ versus relative displacement $(\mathring{u} - \mathring{u}_r)$.

(namely $\varsigma = \sigma_5$, results plotted with red lines); (ii) the *quasi-resonant* case of non-decaying force having imaginary part of the excitation frequency equal to a certain harmonic component of the imaginary spectrum (namely $\mathcal{R}(\varsigma) = 0, \mathcal{I}(\varsigma) = \mathcal{I}(\sigma_5)$, results plotted with black lines); (iii) the *non-resonant* case of non-decaying force having imaginary part of the excitation frequency far from the activable harmonic components of the imaginary spectrum (namely $\mathcal{R}(\varsigma) = 0$, $\mathcal{I}(\varsigma) = 1$, results plotted with blue lines). Clearly, the excitation frequency of the resonant and nearly-resonant cases has been tuned with the imaginary part of the complex wavefrequency σ_5, with the aim of primarily exciting the waveform $\boldsymbol{\varphi}_5$ that is strongly polarized in the relative displacement $(\mathring{v} - \mathring{v}_r)$. As expected, the largest amplitudes of the time-histories are associated to the quasi-resonant case, whose forced response reaches a high-amplitude steady state, after a transient. The mono-harmonic component of the steady state is evidenced by the corresponding FFT, showing a dominant high-amplitude peak at the forcing frequency $\mathcal{I}(\sigma_5)$. The time-histories of the non-resonant case show a qualitatively similar behaviour, with a steady state characterized by significantly lower amplitudes. Furthermore, the different mono-harmonic component is disclosed by the corresponding FFT, showing a dominant but lower-amplitude peak at the forcing frequency $\mathcal{I}(\varsigma)$. Differently, the time-histories of the resonant case do not reach a constant-amplitude steady state, due to the time-decay of the excitation force. Accordingly, the corresponding FFT reveals the same mono-harmonic component of the quasi-resonant case, although with lower amplitude of the dominant frequency peak. Consistently, the quasi-resonant case shows also the largest energy dissipation in the oscillation cycles of the viscoelastic force versus the relative displacement at the steady state.

Since a few wavevectors actually satisfy the condition of full decoupling $\mathcal{C}_{123}$, it is interesting to investigate the forced response for wavevectors providing full coupling (see Fig.2b). To this end, the harmonic punctual force characterized by monocomponent amplitude vector $\boldsymbol{\psi}_v$ is applied in combination with the fixed wavevector $\mathbf{b}_{12}$. Due to the full coupling provided by the out-of-diagonal terms of the stiffness matrix

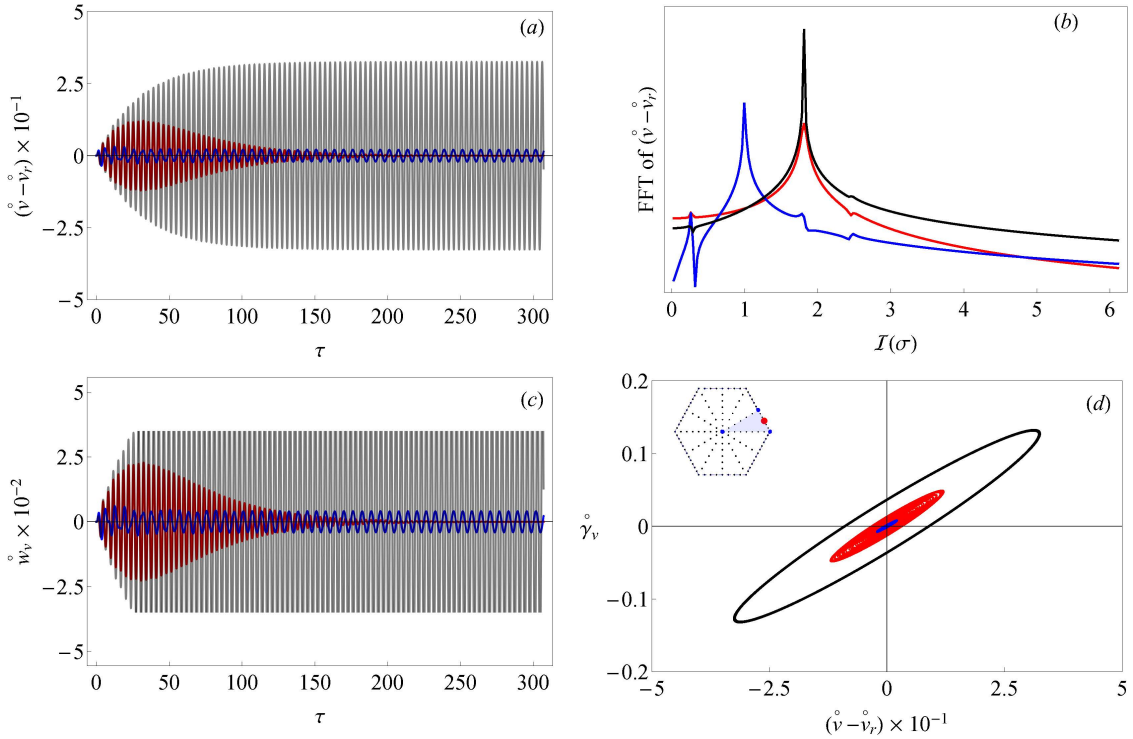

Figure 12: Forced response to harmonic punctual force characterized by monocomponent amplitude vector $\boldsymbol{\psi}_v$ (not-null component $\psi_v = 5 \times 10^{-2}$) for wavevector $\mathbf{b}_{12}$ in the resonant (red lines), quasi-resonant (black lines) and non-resonant (blue lines) cases: (a), (b) time history and FFT of the relative displacement $(\mathring{v} - \mathring{v}_r)$; (c) time history of the viscoelastic state $\mathring{w}_v$; (d) oscillation cycles of viscoelastic force $\mathring{\gamma}_v$ versus relative displacement $(\mathring{v} - \mathring{v}_r)$.

$\boldsymbol{\Sigma}(\mathbf{b}_{12})$, all the waveforms $\boldsymbol{\varphi}_1$-$\boldsymbol{\varphi}_6$ are activated by the external excitation and all the degrees of freedom participate in the forced response. The real-valued relative displacements $(\mathring{u} - \mathring{u}_r)$ and $(\mathring{v} - \mathring{v}_r)$, are illustrated in Fig. 11 and Fig. 12, respectively. The relative rotations $(\mathring{\phi} - \mathring{\phi}_r)$ are instead imaginary-valued due to the complex-valued coupling terms $\Sigma_{12} = -\Sigma_{21}$ and $\Sigma_{13} = -\Sigma_{31}$ in the stiffness matrix. The relevant cases of resonant (red lines), quasi-resonant (black lines) and non-resonant (blue lines) forcing excitation are investigated. From the qualitative viewpoint, all the responses show the typical mono-harmonic oscillations characterized – after a certain transient – by a high-amplitude steady state (quasi-resonant excitation), a low-amplitude steady state (non resonant excitation), an exponential time decay with absence of steady state (resonant excitation). From the quantitative viewpoint, the relative displacements $(\mathring{u} - \mathring{u}_r)$ and $(\mathring{v} - \mathring{v}_r)$ reach comparable oscillation amplitudes, associated to rather similar amplitudes of the viscoelastic states $\mathring{w}_u$, $\mathring{w}_v$ corresponding to similar performances in terms of dissipated energy. On the contrary, the relative rotation $(\mathring{\phi} - \mathring{\phi}_r)$, here not illustrated for the sake of synthesis, is found to reach oscillation amplitudes significantly lower, corresponding to negligible energy dissipation.

A thorough investigation concerning the effects of a variable wavevector $\mathbf{b}$ can be performed by spanning the whole first hexagonal Brillouin zone. To this purpose, the maximum amplitude of the forced response to the harmonic punctual force characterized by monocomponent amplitude vector $\boldsymbol{\psi}_v$ is illustrated in Fig. 13. The cases of complex-valued excitation frequency $\varsigma = \sigma_5$ and imaginary-valued excitation frequencies $\varsigma = \mathcal{I}(\sigma_5)$ or $\varsigma = \imath$ are presented (where σ_5 is evaluated at the wavevector $\mathbf{b}_{12}$). From the qualitative viewpoint, it can be recognized that the maximum amplitudes of the forced response respect the centrosymmetry in the Brillouin zone for all the relative displacements and rotations. From the quantitative viewpoint, the amplitudes grow up everywhere resonance or quasi-resonance conditions occur between the excitation frequency and one of the complex-valued spectral frequencies for a certain wavevector $\mathbf{b}$, as expected.

Having investigated parametrically the effects of a non-null real part of the excitation frequency (red versus black curves in Fig. 11 and Fig. 12) and the consequences of a variable wavevector (Fig. 13), the

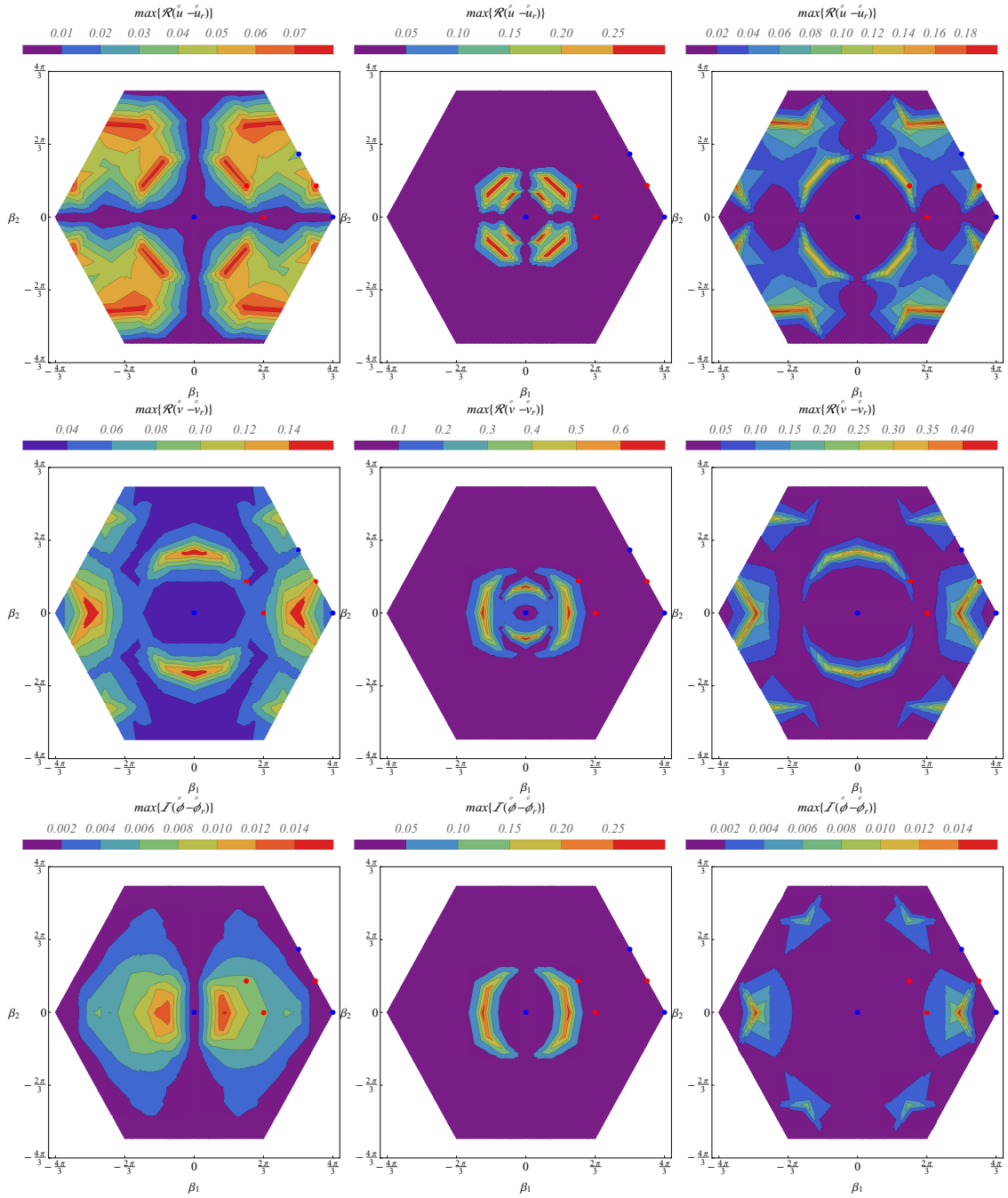

Figure 13: Maximum amplitudes of the forced response to harmonic punctual force characterized by monocomponent amplitude vector $\boldsymbol{\psi}_v$ (not-null component $\psi_v = 5 \times 10^{-2}$): (a) relative displacement $(\mathring{u} - \mathring{u}_r)$, (b) relative displacement $(\mathring{v} - \mathring{v}_r)$, (c) relative rotation $(\mathring{\phi} - \mathring{\phi}_r)$. Excitation frequencies $\varsigma = \sigma_5$ (left), $\varsigma = \mathcal{I}(\sigma_5)$ (center), $\varsigma = \imath$ (right).

dependence of the forced response on different amplitude vectors $\boldsymbol{\varphi}$ for large ranges of the excitation frequency ς remains to be discussed. To this end, three monocomponent amplitude vectors $\boldsymbol{\psi}_u$ (with not-null component $\psi_u = 5 \times 10^{-2}$) and $\boldsymbol{\psi}_v$ (with not-null component $\psi_v = 5 \times 10^{-2}$) are considered. The maximum amplitudes of the forced response are illustrated over the full range of the reduced wavevector ξ for a significant range of purely imaginary excitation frequencies ς. Specifically, the relative displacements and rotations for the amplitude vector $\boldsymbol{\psi}_u$ are illustrated in Fig. 14 for the excitation frequencies range $\mathcal{I}(\varsigma) \in [0.55, 2.65]$.

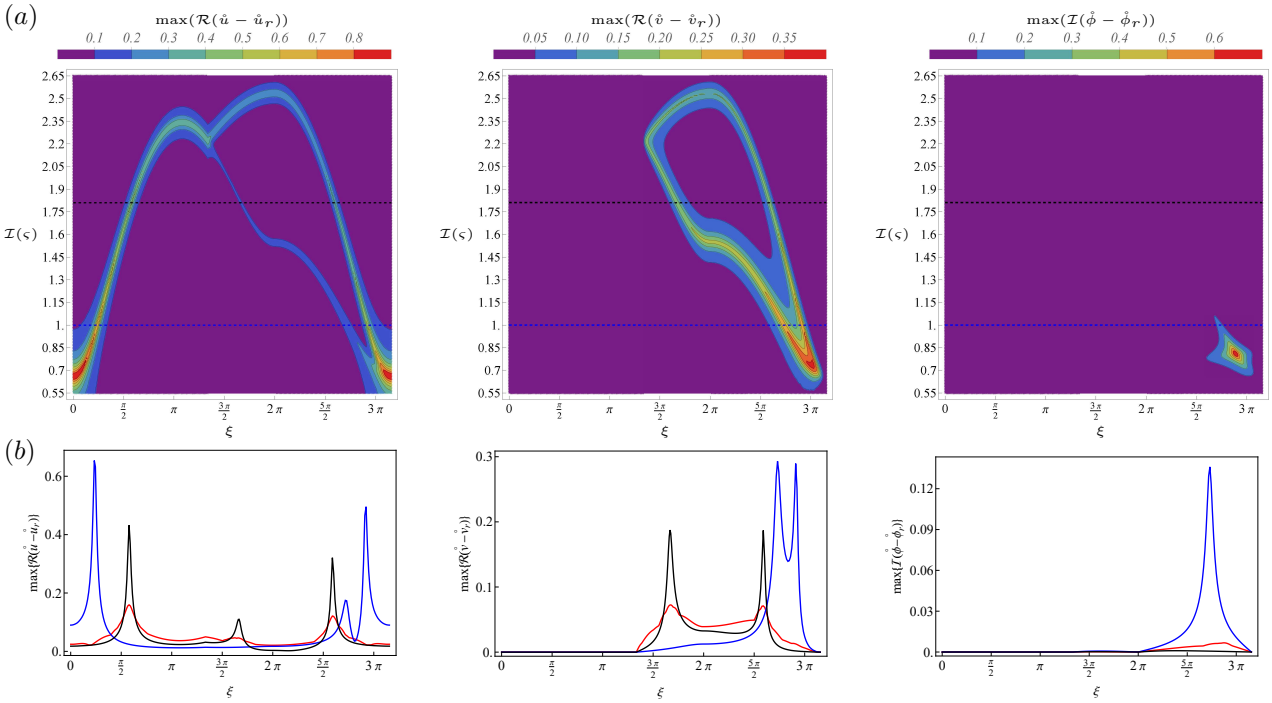

Figure 14: Forced response to harmonic punctual force characterized by monocomponent amplitude vector $\boldsymbol{\psi}_u$ (not-null component $\psi_v = 5 \times 10^{-2}$): (a) maximum amplitudes in the $(\xi, \mathcal{I}(\varsigma))$-plane, (b) maximum amplitudes versus the reduced wavevector for fixed excitation frequencies $\mathcal{I}(\varsigma)$.

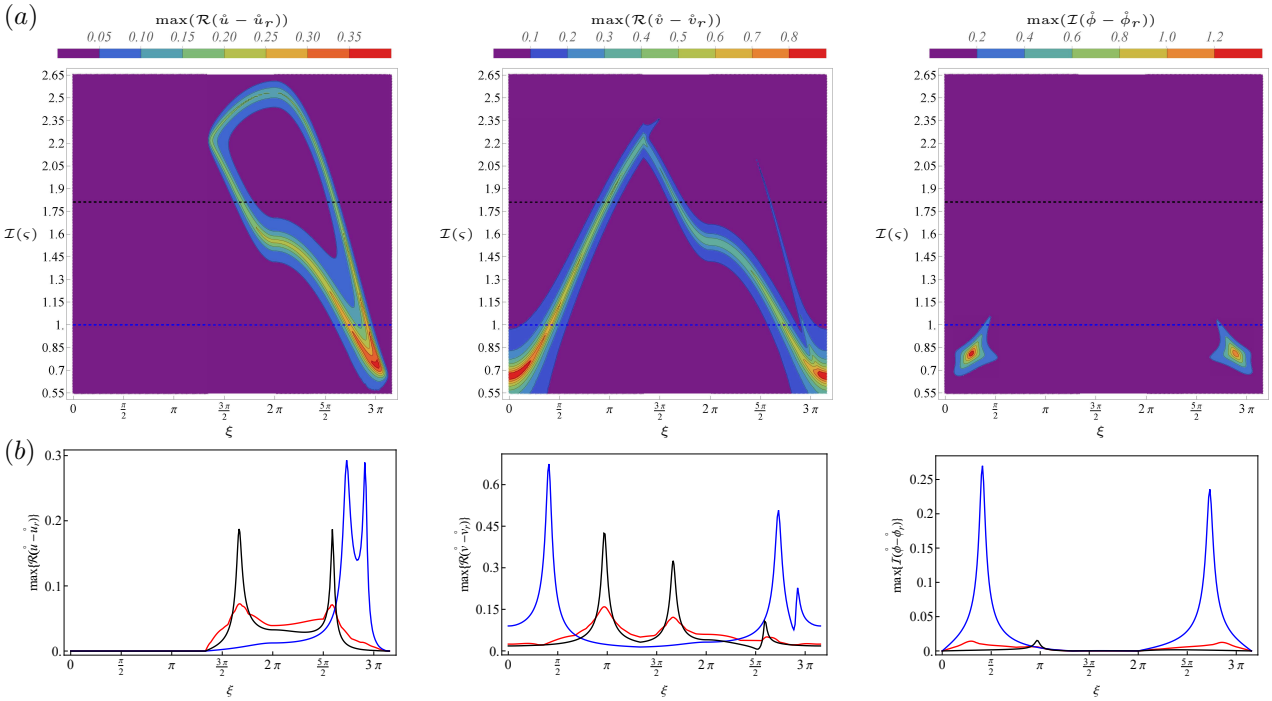

Figure 15: Forced response to harmonic punctual force characterized by monocomponent amplitude vector $\boldsymbol{\psi}_v$ (not-null component $\psi_v = 5 \times 10^{-2}$): (a) maximum amplitudes in the $(\xi, \mathcal{I}(\varsigma))$-plane, (b) maximum amplitudes versus the reduced wavevector for fixed excitation frequencies $\mathcal{I}(\varsigma)$.

It can be recognized how quasi-resonances, causing large but finite amplitudes (not-purple crests), occur in correspondence of the spectral branches associated to activable waveforms (Fig. 14a). To exemplify, the activable waveforms over the range $\xi \in [0, \beta_c \csc(\pi/3)]$, in which the decoupling conditions $\mathcal{C}_{12}$ and $\mathcal{C}_{13}$ are satisfied, are those participated by the relative displacement $(\mathring{u} - \mathring{u}_r)$. Curves illustrating the maximum amplitude versus reduced wavevector are also illustrated in Fig. 14b, considering a pair of fixed excitation frequencies (dashed lines in Fig. 14a). The Figure highlights the different number and positions of the response peaks, depending on the quasi-resonance conditions generated by different excitation frequencies (black and blue curves). Analogous considerations can be pointed out for the relative displacements and rotations of the response to external force with amplitude vector $\boldsymbol{\psi}_u$, illustrated in Fig. 15.

7. Conclusions

Following a variational energetic approach, a general physical-mathematical formulation has been presented to describe the linear dynamics of mechanical metamaterials. Specifically, a parametric beam lattice model has been formulated for the large class of two-dimensional unbounded media characterized by a periodic microstructure. In particular, the model formulation holds for cellular non-dissipative microstructures artificially made by a geometrically repetitive pattern of circular rings, in which each ring is radially interconnected with the nearest neighborhoods by a generic number of rectilinear ligaments (coordination number). The configurational lattice nodes coincide with the equispaced centroids of the stiff and heavy rings, modeled as massive rigid bodies. Nodes can exchange intercellular forces (attraction/repulsion, shear and moment) through the flexible and light ligaments, modeled as massless unshearable beams. The beam lattice model has been enriched by introducing the microstructural dynamic interactions provided by intra-ring tunable oscillators, viscoelastically coupled with the hosting rings to realize damped local resonators. As peculiar aspect, the viscoelastic ring-resonator coupling has been derived by a consistent mathematical formulation based on the Boltzmann superposition integral, whose kernel can be expressed by a Prony series.

According to the model assumptions, the forced dynamics of the beam lattice model are initially governed by a system of ordinary integral-differential equations. As primary methodological development with respect to previous studies, the dynamic state space has been enlarged by adding auxiliary internal variables (intracellular viscoelastic states), whose coupled linear dynamics are governed by first-order linear differential equations. According to this strategy, the model dimension grows proportionally to the terms of the Prony series, but can be conveniently described by a system of ordinary differential equations. Considering a generic number of added viscoelastic states, the $\mathcal{Z}$-transform and a suitable mapping in the wavevector space have been applied to obtain the system of ordinary differential equations governing the free and forced propagation of damped waves. From the methodological viewpoint, this mathematical approach can be considered a valid alternative to the common application of the quasi-periodicity conditions according to the Floquet-Bloch theory. First, a fully-analytical procedure has been outlined to solve the propagation problem of generically forced waves, by attacking the governing differential equations in the time domain. Second, the polynomial algebraic eigenproblem governing the free propagation of harmonic damped waves in the complex frequency domain has been stated by applying the bilateral Laplace transform. In this respect, the enlargement of the state space has been proved to profitably circumvent the algorithmic necessity of de-rationalizing or asymptotically approximating the characteristic equation.

The triangular beam lattice metamaterial has been selected as prototypical reference model for illustrating the theoretical and methodological developments. The governing equations of motion have been derived by considering the lowest two terms of the Prony series, corresponding to the minimal enlargement of the state space. Considering first the free wave propagation, the structural properties of the quasi-symmetric dynamic stiffness matrix have been discussed up to identifying the wavevector loci that realize the strongest and weakest (null) coupling among the relative ring-resonator displacements participating in the waveforms. This investigation opens interesting perspectives in the management of the mechanical energy transferred by strongly polarized propagating waves. Therefore, the dispersion frequency spectrum has been parametrically investigated in the space of real-valued wavevectors and complex-valued frequencies, with focus on the spectral effects of the viscoelastic coupling. As major qualitative remark, the addition of viscoelastic states determines a relevant enrichment of the dispersion spectrum, which shows the typical complex-valued

branches corresponding to propagating damped waves, but also extra real-valued branches corresponding to standing (non-propagating) waves. As complementary quantitative remark, the viscosity-related effect of amplitude widening/narrowing in the pass and stop band structure has been highlighted, with respect to non-dissipative metamaterials with the same microstructure. Significantly, the spectral damping ratio of propagating waves has been verified to attain a wavevector-dependent maximum, for a particular value of the relaxation time ruling the viscoelastic coupling. This particular finding paves the way for stating spectral design problems targeted at optimizing the viscoelastic properties for the maximization of the dissipated energy. Moreover, the dependence of the stop bandwidth amplitude between the low and high-frequency spectral branches on the relaxation time characterizing the viscous function has also been highlighted and discussed. Finally, considering the forced wave propagation, the response to harmonically decaying and non-decaying excitations, given by an external mono-frequency point force, has been investigated. The metamaterial response has been determined numerically in the time domain. Considerations regarding the participation of one or the other waveforms have been pointed out, on the basis of the stronger or weaker conditions of internal coupling occurring at different wavevectors. Spanning a large range of excitation frequency has allowed to qualitatively compare and quantitatively discuss the results by distinguishing the fundamental cases of no-resonance, resonance and quasi-resonance, respectively.

Appendix A. Formulation with added states

Given the convolution expression of the time-dependent function $F(t)$

$$F(t) = F_0 \int_{-\infty}^{t} \Phi(t-t_*)\partial_{t_*}\xi(t_*)\,dt_*, \tag{A.1}$$

where t_* is an auxiliary time variable, ξ is a generic casual time-dependent dynamic state, $\Phi(t-t_*)$ is a continuous and differentiable function of times t and t_* and ∂_{t_*} represents partial differentiation with respect to the auxiliary time t_*. By assuming $\xi = 0$ when $t < 0$ for all casual time-dependent dynamic states ξ, and since $\Phi(t-t_*) = 0$ for $t < t_*$, then Eq. (A.1) becomes

$$F(t) = F_0 \left[\Phi(t)\xi(0) + \int_{0}^{t} \Phi(t-t_*)\partial_{t_*}\xi(t_*)\,dt_*\right]. \tag{A.2}$$

Integrating by part the convolution integral in (A.2), the function $F(t)$ can be expressed as

$$F(t) = F_0 \left\{\Phi(t)\xi(0) + \big[\Phi(0)\xi(t) - \Phi(t)\xi(0)\big] - \int_{0}^{t} \partial_{t_*}\Phi(t-t_*)\xi(t_*)\,dt_*\right\}, \tag{A.3}$$

which simplifies as

$$F(t) = F_0 \left[\Phi(0)\xi(t) - \int_{0}^{t} \partial_{t_*}\Phi(t-t_*)\xi(t_*)\,dt_*\right]. \tag{A.4}$$

In the particular case in which the function $\Phi(t-t_*)$ is a series of exponential functions

$$\Phi(t-t_*) = 1 - \sum_{i=1}^{N} a_i e^{-b_i(t-t_*)}, \tag{A.5}$$

where a_i and b_i are constant coefficient terms of the series, its derivative with respect to time t_* can be calculated as

$$\partial_{t_*}\Phi(t-t_*) = -\sum_{i=1}^{N} a_i b_i e^{-b_i(t-t_*)}. \tag{A.6}$$

By introducing, for the sake of notational simplicity, the function $\varphi_i(t-t_*) := e^{-b_i(t-t_*)}$ representative of the ith term of the series, then Eqs. (A.5) and (A.6) can be rewritten in the more compact form as

$$\Phi(t-t_*) = 1 - \sum_{i=1}^{N} a_i\varphi_i(t-t_*),\ \ \partial_{t_*}\Phi(t-t_*) = -\sum_{i=1}^{N} a_i b_i\varphi_i(t-t_*), \tag{A.7}$$

respectively; hence, the convolution integral in Eq. (A.4) can be written as

$$\int_0^t \partial_{t_*}\Phi(t-t_*)\xi(t_*)\,dt_* = -\sum_{i=1}^{N} a_i b_i \int_0^t \varphi_i(t-t_*)\xi(t_*)\,dt_*\,. \tag{A.8}$$

By denoting by W_i the ith additional dynamic variable defined as

$$W_i(t) := \int_0^t \varphi_i(t-t_*)\xi(t_*)\,dt_*\,, \tag{A.9}$$

then Eq. (A.8) becomes:

$$\int_0^t \partial_{t_*}\Phi(t-t_*)\xi(t_*)\,dt_* = -\sum_{i=1}^{N} a_i b_i W_i(t)\,. \tag{A.10}$$

By enforcing the differentiation properties of the convolution integral, the derivative with respect to time t of the ith additional dynamic variable W_i can be written as

$$\dot{W}_i(t) = \varphi_i(0)\xi(t) + \int_0^t \dot{\varphi}_i(t-t_*)\xi(t_*)\,dt_*\,, \tag{A.11}$$

where the overdot indicates derivative with respect to time t. The derivative with respect to time t of the function $\varphi_i(t-t_*)$ reads $\dot{\varphi}_i(t-t_*) = -b_i e^{-b_i(t-t_*)}$; therefore, due to the definition of the function $\varphi_i(t-t_*)$, its time derivative can be written as

$$\dot{\varphi}_i(t-t_*) = -b_i\varphi_i(t-t_*)\,. \tag{A.12}$$

Hence, Eq. (A.11) becomes

$$\dot{W}_i(t) = \varphi_i(0)\xi(t) - b_i \int_0^t \varphi_i(t-t_*)\xi(t_*)\,dt_*\,, \tag{A.13}$$

where, due to the definition provided in Eq. (A.9), the integral in the right hand side of Eq. (A.13) is the additional dynamic state $W_i(t)$ and Eq. (A.13) can be then written in the more compact form as:

$$\dot{W}_i(t) + b_i W_i(t) - \varphi_i(0)\xi(t) = 0\,, \tag{A.14}$$

which represents the first-order differential equation governing the dynamics of the additional $i$the dynamic state $W_i(t)$. Finally, being $\Phi(0) = 1 - \sum_{i=1}^{N} a_i$, the function $F(t)$ can be written as a linear combination of the N dynamic states as:

$$F(t) = F_0\left[\left(1 - \sum_{i=1}^{N} a_i\right)\xi(t) + \sum_{i=1}^{N} a_i b_i W_i(t)\right]\,, \tag{A.15}$$

whose dynamics, since $\varphi_i(0) = 1$, are governed by the N differential equations

$$\dot{W}_i(t) + b_i W_i(t) - \xi(t) = 0\ , i = 1,\dots,N\,. \tag{A.16}$$

Appendix B. Governing matrices

The augmented $(6+3N)$-by-$(6+3N)$ stiffness matrix $\tilde{\mathbf{K}}$ multiplying the $\mathbf{k}$-mapped $\mathcal{Z}$-transformed displacements $\mathring{\mathbf{q}}(t,\mathbf{k})$ in Eq.(24) reads

$$\tilde{\mathbf{K}}(\mathbf{k}) = \begin{bmatrix} (\mathbf{I}+\mathbf{S})\,\mathbf{K}_e + \mathbf{H}(\mathbf{k}) & -(\mathbf{I}+\mathbf{S})\,\mathbf{K}_e & \dots & -\mathbf{T}_N\mathbf{D}_N\mathbf{K}_e \\ -(\mathbf{I}+\mathbf{S})\,\mathbf{K}_e & (\mathbf{I}+\mathbf{S})\,\mathbf{K}_e & \dots & \mathbf{T}_N\mathbf{D}_N\mathbf{K}_e \\ \vdots & \vdots & \ddots & \vdots \\ -\mathbf{I} & \mathbf{I} & \dots & \mathbf{T}_N \end{bmatrix}\,. \tag{B.1}$$

The nondimensional 9-by-9 matrix $\mathbf{\Gamma}(\sigma,\mathbf{b})$ in Eq.(30) governing the dynamics of the triangular beam lattice metamaterial in the frequency domain reads

$$\mathbf{\Gamma}(\sigma,\mathbf{b}) = \begin{bmatrix} \sigma^2\,\mathbf{\Pi}_a + (\mathbf{I}+\mathbf{D})\,\mathbf{\Sigma}_e + \mathbf{\Xi}(\mathbf{b}) & -(\mathbf{I}+\mathbf{D})\,\mathbf{\Sigma}_e & -\mathbf{\Omega}\,\mathbf{D}\,\mathbf{\Sigma}_e \\ -(\mathbf{I}+\mathbf{D})\,\mathbf{\Sigma}_e & \sigma^2\,\mathbf{\Pi}_r + (\mathbf{I}+\mathbf{D})\,\mathbf{\Sigma}_e & \mathbf{\Omega}\,\mathbf{D}\,\mathbf{\Sigma}_e \\ -\mathbf{\Omega}\,\mathbf{D}\,\mathbf{\Sigma}_e & \mathbf{\Omega}\,\mathbf{D}\,\mathbf{\Sigma}_e & (\sigma\,\mathbf{I}+\mathbf{\Omega})\,\mathbf{\Omega}\,\mathbf{D}\,\mathbf{\Sigma}_e \end{bmatrix} \tag{B.2}$$

while the nondimensional 9-by-9 matrix $\mathbf{\Sigma}(\mathbf{b})$ in Eq.(33) governing the forced dynamics of the triangular beam lattice metamaterial in the time domain reads

$$\mathbf{\Sigma}(\mathbf{b}) = \begin{bmatrix} (\mathbf{I}+\mathbf{D})\,\mathbf{\Sigma}_e + \mathbf{\Xi}(\mathbf{b}) & -(\mathbf{I}+\mathbf{D})\,\mathbf{\Sigma}_e & -\mathbf{\Omega}\,\mathbf{D}\,\mathbf{\Sigma}_e \\ -(\mathbf{I}+\mathbf{D})\,\mathbf{\Sigma}_e & (\mathbf{I}+\mathbf{D})\,\mathbf{\Sigma}_e & \mathbf{\Omega}\,\mathbf{D}\,\mathbf{\Sigma}_e \\ -\mathbf{\Omega}\,\mathbf{D}\,\mathbf{\Sigma}_e & \mathbf{\Omega}\,\mathbf{D}\,\mathbf{\Sigma}_e & \mathbf{\Omega}\,\mathbf{\Omega}\,\mathbf{D}\,\mathbf{\Sigma}_e \end{bmatrix} \tag{B.3}$$

where $\mathbf{\Pi}_a = \mathrm{diag}\,(1,1,\chi^2)$ and $\mathbf{\Pi}_r = \mathrm{diag}\,(\varrho^2,\varrho^2,\chi_r^2)$ are the nondimensional mass matrices of the ring and the resonator, respectively, while $\mathbf{\Sigma}_e = \mathrm{diag}\,(\kappa_u,\kappa_v,\kappa_\phi)$ is the nondimensional coupling stiffness matrix, and $\mathbf{\Omega} = \tau_r^{-1}\mathbf{I}$ is the nondimensional matrix accounting for the relaxation time. Finally $\mathbf{\Xi}(\mathbf{b})$ is the nondimensional representation of the 3-by-3 Hermitian matrix $\mathbf{H}(\mathbf{k})$, and its components read

$$\begin{aligned}
&\Xi_{11}(\mathbf{b}) = 3 + 36\mu^2 - 2c_0(\mathbf{b}) - \left(1+36\mu^2\right)c_1(\mathbf{b}),\\
&\Xi_{22}(\mathbf{b}) = 3 + 36\mu^2 - 24\mu^2 c_0(\mathbf{b}) - 3\left(1+4\mu^2\right)c_1(\mathbf{b}),\\
&\Xi_{22}(\mathbf{b}) = 4\mu^2\left[6\left(1+3\chi+3\chi^2\right) + \left(1+6\chi+6\chi^2\right)\left(c_0(\mathbf{b}) + 2\,c_1(\mathbf{b})\right)\right],\\
&\Xi_{12}(\mathbf{b}) = \Xi_{21}(\mathbf{b}) = \left(1-12\mu^2\right)c_2(\mathbf{b})\tan(\pi/3),\\
&\Xi_{13}(\mathbf{b}) = -\Xi_{31}(\mathbf{b}) = -\imath 12\mu^2\left(1+2\chi\right)c_3(\mathbf{b})\tan(\pi/3),\\
&\Xi_{23}(\mathbf{b}) = -\Xi_{32}(\mathbf{b}) = \imath\,12\mu^2\left(1+2\chi\right)\left(c_4(\mathbf{b}) + 2c_5(\mathbf{b})\right),
\end{aligned} \tag{B.4}$$

where the auxiliary trigonometric functions $c_0(\mathbf{b}) = \cos\beta_1$, $c_1(\mathbf{b}) = \cos\left(\frac{1}{2}\beta_1\right)\cos\left(\frac{1}{2}\beta_2\tan(\pi/3)\right)$, $c_2(\mathbf{b}) = \sin\left(\frac{1}{2}\beta_1\right)\sin\left(\frac{1}{2}\beta_2\tan(\pi/3)\right)$, $c_3(\mathbf{b}) = \cos\left(\frac{1}{2}\beta_1\right)\sin\left(\frac{1}{2}\beta_2\tan(\pi/3)\right)$, $c_4(\mathbf{b}) = \sin\left(\frac{1}{2}\beta_1\right)\cos\left(\frac{1}{2}\beta_2\tan(\pi/3)\right)$, $c_5(\mathbf{b}) = \sin\left(\frac{1}{2}\beta_1\right)\cos\left(\frac{1}{2}\beta_1\right)$ have been introduced. It is worth noting that, since $\mathbf{\Pi}$, $\mathbf{D}$, $\mathbf{\Sigma}_e$ are diagonal matrices, the relations $\Gamma_{12}(\sigma,\mathbf{b}) = \Sigma_{12}(\mathbf{b}) = \Xi_{12}(\mathbf{b})$, $\Gamma_{13}(\sigma,\mathbf{b}) = \Sigma_{13}(\mathbf{b}) = \Xi_{13}(\mathbf{b})$, $\Gamma_{23}(\sigma,\mathbf{b}) = \Sigma_{23}(\mathbf{b}) = \Xi_{23}(\mathbf{b})$ hold.

Appendix C. Forced response in the time domain

The ordinary differential equations of motion (24) governing the forced response of the mechanical metamaterial in the time domain and the reciprocal space can be expressed as a first-order linear dynamic system $\mathbf{A}(\mathring{\mathbf{x}})^{\cdot} + \mathbf{B}\mathring{\mathbf{x}} = \mathring{\mathbf{b}}$, by defining the $(\mathbf{k},t)$-dependent vector variables $\mathring{\mathbf{x}} = [(\mathring{\mathbf{u}})^{\cdot}, \mathring{\mathbf{u}}, (\mathring{\mathbf{v}})^{\cdot}, \mathring{\mathbf{v}}, ..., \mathring{\mathbf{w}}_{N_k}]^\top$ and $\mathring{\mathbf{b}} = [\mathring{\mathbf{f}}, \mathbf{0}, \mathbf{0}, \mathbf{0}, ..., \mathbf{0}]^\top$ and introducing the $(12+3N_k)$-by-$(12+3N_k)$ matrix $\mathbf{A} = \mathrm{diag}(\mathbf{M}, \mathbf{I}, \mathbf{M}_r, \mathbf{I}, \mathbf{I}, ..., \mathbf{I}_N)$ and the $\mathbf{k}$-dependent $(12+3N_k)$-by-$(12+3N_k)$ matrix

$$\mathbf{B}(\mathbf{k}) = \begin{bmatrix} \mathbf{O} & (\mathbf{I}+\mathbf{S})\mathbf{K}_e + \mathbf{H}(\mathbf{k}) & \mathbf{O} & -(\mathbf{I}+\mathbf{S})\mathbf{K}_e & ... & -\mathbf{T}_{N_k}\mathbf{D}_{N_k}\mathbf{K}_e \\ -\mathbf{I} & \mathbf{O} & \mathbf{O} & \mathbf{O} & ... & \mathbf{O} \\ \mathbf{O} & -(\mathbf{I}+\mathbf{S})\mathbf{K}_e & \mathbf{O} & (\mathbf{I}+\mathbf{S})\mathbf{K}_e & ... & \mathbf{T}_{N_k}\mathbf{D}_{N_k}\mathbf{K}_e \\ \mathbf{O} & \mathbf{O} & -\mathbf{I} & \mathbf{O} & ... & \mathbf{O} \\ ... & ... & ... & ... & ... & ... \\ \mathbf{O} & -\mathbf{I} & \mathbf{O} & \mathbf{I} & ... & \mathbf{T}_{N_k} \end{bmatrix} \tag{C.1}$$

and, since the matrix $\mathbf{A}$ is invertible (being $\det\mathbf{A} = \frac{1}{2}M^3M_r^3R^2R_r^2$), the system can suitably be cast in the form $(\mathring{\mathbf{x}})^{\cdot} - \mathbf{J}(\mathbf{k})\mathring{\mathbf{x}} = \mathring{\mathbf{c}}$, where $\mathbf{J}(\mathbf{k}) = -\mathbf{A}^{-1}\mathbf{B}(\mathbf{k})$ and $\mathring{\mathbf{c}} = \mathbf{A}^{-1}\mathring{\mathbf{b}}$. The solution can formally be expressed as

$$\mathring{\mathbf{x}}(t,\mathbf{k}) = \exp\left[(t-t_0)\,\mathbf{J}(\mathbf{k})\right]\mathring{\mathbf{x}}_0(\mathbf{k}) + \int_{t_0}^{t}\exp\left[(t-t_*)\,\mathbf{J}(\mathbf{k})\right]\mathring{\mathbf{c}}(t_*,\mathbf{k})\mathrm{d}t_* \tag{C.2}$$

where it may be worth recalling the definition of exponential of the matrix

$$\exp\left[(t-t_0)\,\mathbf{J}(\mathbf{k})\right] = \sum_{\ell=0}^{\infty} \frac{1}{\ell\,!}\left[\mathbf{J}(\mathbf{k})\,(t-t_0)\right]^{\ell}, \tag{C.3}$$

and the initial conditions read $\mathring{\mathbf{x}}_0(\mathbf{k}) = \mathring{\mathbf{x}}(t=t_0,\mathbf{k})$. Recalling equation (23) and the mapping rule $z_j = \exp(\imath\, B\mathbf{n}_j\cdot\mathbf{k})$, the matrix $\mathbf{H}(\mathbf{k})$ can be written

$$\mathbf{H}(\mathbf{k}) = \mathbf{H}_0 + \sum_{j=1}^{n/2}\mathbf{H}_j^{-}\exp(-\imath\, B\mathbf{n}_j\cdot\mathbf{k}) + \sum_{j=1}^{n/2}\mathbf{H}_j^{+}\exp(\imath\, B\mathbf{n}_j\cdot\mathbf{k}), \tag{C.4}$$

where the $\mathbf{k}$-independent matrices $\mathbf{H}_0 = \mathbf{K}^{-}+\mathbf{K}^{+}$, $\mathbf{H}_j^{-} = (\mathbf{B}_j^{-})^{\top}\mathbf{\Theta}_j^{\top}\mathbf{K}\,\mathbf{\Theta}_j\,\mathbf{B}_j^{+}$, $\mathbf{H}_j^{+} = (\mathbf{B}_j^{+})^{\top}\mathbf{\Theta}_j^{\top}\mathbf{K}\,\mathbf{\Theta}_j\,\mathbf{B}_j^{-}$ are introduced. Accordingly, the $\mathbf{H}(\mathbf{k})$-dependent matrix $\mathbf{J}(\mathbf{k})$ can be expressed as

$$\mathbf{J}(\mathbf{k}) = \mathbf{J}_0 + \sum_{j=1}^{n/2}\mathbf{J}_j^{-}\exp(-\imath\, B\mathbf{n}_j\cdot\mathbf{k}) + \sum_{j=1}^{n/2}\mathbf{J}_j^{+}\exp(\imath\, B\mathbf{n}_j\cdot\mathbf{k}) = \sum_{j=-n/2}^{n/2}\mathbf{J}_j\exp(\imath\, B\mathbf{n}_j\cdot\mathbf{k}\,h[j]), \tag{C.5}$$

where $h[j] = 2H[j]-1$ depends on the discrete Heaviside function $H[j]$. The definition of the exponential matrix in (C.3) requires the assessment of the ℓ-power of the $\mathbf{J}(\mathbf{k})$, which can be determined as

$$\mathbf{J}(\mathbf{k})^{\ell} = \sum_{r_1+\ldots+r_{n+1}=\ell}\binom{\ell}{r_1,\ldots,r_{n+1}}\prod_{j=1}^{n+1}\left[\mathbf{J}_j\exp(\imath\, B\mathbf{n}_j\cdot\mathbf{k}\,h[j])\right]^{r_j} \tag{C.6}$$

where $r_1,\ldots,r_{n+1}\in\mathbb{N}^*$ in the binomial coefficient. Therefore, by substituting equation (C.6) into equation (C.3), the solution (C.2) is

$$\begin{aligned}\mathring{\mathbf{x}}(t,\mathbf{k}) = &\left[\sum_{\ell=0}^{\infty}\frac{1}{\ell\,!}\,(t-t_0)^{\ell}\sum_{r_1+\ldots+r_{n+1}=\ell}\binom{\ell}{r_1,\ldots,r_{n+1}}\prod_{j=1}^{n+1}\left[\mathbf{J}_j\exp(\imath\, B\mathbf{n}_j\cdot\mathbf{k}\,h[j])\right]^{r_j}\right]\mathring{\mathbf{x}}_0(\mathbf{k}) + \\ &+\sum_{\ell=0}^{\infty}\frac{1}{\ell\,!}\int_{t_0}^{t}(t-t_*)^{\ell}\left[\sum_{r_1+\ldots+r_{n+1}=\ell}\binom{\ell}{r_1,\ldots,r_{n+1}}\prod_{j=1}^{n+1}\left[\mathbf{J}_j\exp(\imath\, B\mathbf{n}_j\cdot\mathbf{k}\,h[j])\right]^{r_j}\right]\mathring{\mathbf{c}}(t_*,\mathbf{k})\mathrm{d}t_*\end{aligned} \tag{C.7}$$

where the order of integration and sum has been inverted by virtue of the series convergence. Finally, by applying the inverse discrete Fourier transform, the solution in the physical space is determined as

$$\mathbf{x}_{\mathcal{J}}(t) = \mathcal{F}_d^{-1}[\mathring{\mathbf{x}}(t,\mathbf{k})] = \frac{1}{|\mathcal{B}|}\int_{\mathcal{B}}\mathring{\mathbf{x}}(t,\mathbf{k})\prod_{j=1}^{n/2}\exp[\imath(i_j-1)(B\mathbf{n}_j\cdot\mathbf{k})]\mathrm{d}\mathbf{k} \tag{C.8}$$

where $|\mathcal{B}|$ is the size of the first Brillouin zone.

Acknowledgments

The authors gratefully acknowledge financial support from National Group of Mathematical Physics (GNFM-INdAM), from the Compagnia San Paolo, project MINIERA no. I34I20000380007 and from University of Trento, project UNMASKED 2020.

References

[1] Fleck, N., Deshpande, V., and Ashby, M. (2010). Micro-architectured materials: past, present and future. *Proceedings of the Royal Society of London A: Mathematical, Physical and Engineering Sciences*, 466(2121):2495–2516.

[2] Kadic, M., Milton, G. W., van Hecke, M., and Wegener, M. (2019). 3d metamaterials. *Nature Reviews Physics*, 1:198–210.

[3] Hussein, M. I., Leamy, M. J., and Ruzzene, M. (2014). Dynamics of phononic materials and structures: Historical origins, recent progress, and future outlook. *Applied Mechanics Reviews*, 66(4):040802.

[4] Ferreira, A. D. B., Nóvoa, P. R., and Marques, A. T. (2016). Multifunctional material systems: a state-of-the-art review. *Composite Structures*, 151:3–35.

[5] Zadpoor, A. A. (2020). Meta-biomaterials. *Biomaterials science*, 8(1):18–38.

[6] Jafari, H., Yazdi, M. H., and Fakhrabadi, M. M. S. (2020). Damping effects on wave-propagation characteristics of microtubule-based bio-nano-metamaterials. *International Journal of Mechanical Sciences*, 184:105844.

[7] Lu, M.-H., Feng, L., and Chen, Y.-F. (2009). Phononic crystals and acoustic metamaterials. *Materials today*, 12(12):34–42.

[8] Lee, J.-H., Singer, J. P., and Thomas, E. L. (2012). Micro-/nanostructured mechanical metamaterials. *Advanced materials*, 24(36):4782–4810.

[9] Wu, W., Hu, W., Qian, G., Liao, H., Xu, X., and Berto, F. (2019). Mechanical design and multifunctional applications of chiral mechanical metamaterials: A review. *Materials & Design*, 180:107950.

[10] Jia, Z., Liu, F., Jiang, X., and Wang, L. (2020). Engineering lattice metamaterials for extreme property, programmability, and multifunctionality. *Journal of Applied Physics*, 127(15):150901.

[11] Dirrenberger, J., Forest, S., and Jeulin, D. (2013). Effective elastic properties of auxetic microstructures: anisotropy and structural applications. *International Journal of Mechanics and Materials in Design*, 9(1):21–33.

[12] Colquitt, D. J., Brun, M., Gei, M., Movchan, A. B., Movchan, N. V., and Jones, I. S. (2014). Transformation elastodynamics and cloaking for flexural waves. *Journal of the Mechanics and Physics of Solids*, 72:131–143.

[13] Yang, M. and Sheng, P. (2017). Sound absorption structures: From porous media to acoustic metamaterials. *Annual Review of Materials Research*, 47:83–114.

[14] Bacigalupo, A. and Lepidi, M. (2018). Acoustic wave polarization and energy flow in periodic beam lattice materials. *International Journal of Solids and Structures*, 147:183–203.

[15] D'Alessandro, L., Ardito, R., Braghin, F., and Corigliano, A. (2019). Low frequency 3D ultra-wide vibration attenuation via elastic metamaterial. *Scientific Reports*, 9(1):8039.

[16] Bordiga, G., Cabras, L., Bigoni, D., and Piccolroaz, A. (2019). Free and forced wave propagation in a Rayleigh beam grid: flat bands, Dirac cones, and vibration localization vs isotropization. *International Journal of Solids and Structures*, 161:64–81.

[17] Bacigalupo, A., De Bellis, M. L., and Misseroni, D. (2020). Design of tunable acoustic metamaterials with periodic piezoelectric microstructure. *Extreme Mechanics Letters*, 40:100977.

[18] Hussein, M. I., Patrick, I., Banerjee, A., and Adhikari, S. (2022). Metadamping in inertially amplified metamaterials: Trade-off between spatial attenuation and temporal attenuation. *Journal of Sound and Vibration*, 531:116977.

[19] Christensen, J., Kadic, M., Kraft, O., and Wegener, M. (2015). Vibrant times for mechanical metamaterials. *MRS Communications*, 5(3):453–462.

[20] Bertoldi, K., Vitelli, V., Christensen, J., and Van Hecke, M. (2017). Flexible mechanical metamaterials. *Nature Reviews Materials*, 2(11):1–11.

[21] Yu, X., Zhou, J., Liang, H., Jiang, Z., and Wu, L. (2018). Mechanical metamaterials associated with stiffness, rigidity and compressibility: A brief review. *Progress in Materials Science*, 94:114–173.

[22] Surjadi, J. U., Gao, L., Du, H., Li, X., Xiong, X., Fang, N. X., and Lu, Y. (2019). Mechanical metamaterials and their engineering applications. *Advanced Engineering Materials*, 21(3):1800864.

[23] Dudek, K. K., Martínez, J. A. I., Ulliac, G., and Kadic, M. (2022). Micro-scale auxetic hierarchical mechanical metamaterials for shape morphing. *Advanced Materials*, 34(14):2110115.

[24] Lepidi, M. and Bacigalupo, A. (2018). Parametric design of the band structure for lattice materials. *Meccanica*, 53(3):613–628.

[25] Settimi, V., Lepidi, M., and Bacigalupo, A. (2022). Analytical spectral design of mechanical metamaterials with inertia amplification. *submitted*.

[26] Lepidi, M. and Bacigalupo, A. (2018). Multi-parametric sensitivity analysis of the band structure for tetrachiral acoustic metamaterials. *International Journal of Solids and Structures*, 136-137:186–202.

[27] Settimi, V., Lepidi, M., and Bacigalupo, A. (2021). Nonlinear dispersion properties of one-dimensional mechanical metamaterials with inertia amplification. *International Journal of Mechanical Sciences*, 201:106461.

[28] Bacigalupo, A., Lepidi, M., Gnecco, G., Vadalà, F., and Gambarotta, L. (2019). Optimal design of the band structure for beam lattice metamaterials. *Frontiers in Materials*, 6:2.

[29] Bruggi, M. and Corigliano, A. (2019). Optimal 2D auxetic micro-structures with band gap. *Meccanica*, 54(13):2001–2027.

[30] Li, W., Meng, F., Chen, Y., Li, Y. F., and Huang, X. (2019). Topology optimization of photonic and phononic crystals and metamaterials: A review. *Advanced Theory and Simulations*, 2(7):1900017.

[31] Ronellenfitsch, H., Stoop, N., Yu, J., Forrow, A., and Dunkel, J. (2019). Inverse design of discrete mechanical metamaterials. *Physical Review Materials*, 3(9):095201.

[32] Bacigalupo, A., Gnecco, G., Lepidi, M., and Gambarotta, L. (2020). Machine-learning techniques for the optimal design of acoustic metamaterials. *Journal of Optimization Theory and Applications*, 187(3):630–653.

[33] Gnecco, G. and Bacigalupo, A. (2021). Convex combination of data matrices: PCA perturbation bounds for multi-objective optimal design of mechanical metafilters. *Mathematical Foundations of Computing*, 4(4):253–269.

[34] Bacigalupo, A., Gnecco, G., Lepidi, M., and Gambarotta, L. (2021). Computational design of innovative mechanical metafilters via adaptive surrogate-based optimization. *Computer Methods in Applied Mechanics and Engineering*, 375:113623.

[35] Fortunati, A., Bacigalupo, A., Lepidi, M., Arena, A., and Lacarbonara, W. (2022). Nonlinear wave propagation in locally dissipative metamaterials via Hamiltonian perturbation approach. *Nonlinear Dynamics*, 108:765–787.

[36] Kochmann, D. M., Hopkins, J. B., and Valdevit, L. (2019). Multiscale modeling and optimization of the mechanics of hierarchical metamaterials. *MRS Bulletin*, 44(10):773–781.

[37] Fabrizio, M. and Morro, A. (1992). *Mathematical Problems in Linear Viscoelasticity. Studies in Applied Mathematics*.

[38] Biot, M. (1958). Linear thermodynamics and the mechanics of solids. In *Third U.S. National Congress of Applied Mechanics, ASME*.

[39] Gurtin, M. E. and Sternberg, E. (1962). On the linear theory of viscoelasticity. *Archive for rational mechanics and analysis*, 11(1):291–356.

[40] Roylance, D. (2001). *Engineering viscoelasticity*, volume 2139.

[41] Lakes, R. (2009). *Viscoelastic materials*. Cambridge University Press.

[42] Wagner, N. and Adhikari, S. (2003). Symmetric state-space method for a class of nonviscously damped systems. *AIAA Journal*, 41(5):951–956.

[43] Hussein, M. I. (2009). Theory of damped bloch waves in elastic media. *Physical Review B*, 80(21):212301.

[44] Manimala, J. M. and Sun, C. (2014). Microstructural design studies for locally dissipative acoustic metamaterials. *Journal of Applied Physics*, 115(2):023518.

[45] Lewińska, M., Kouznetsova, V., Van Dommelen, J., Krushynska, A., and Geers, M. (2017). The attenuation performance of locally resonant acoustic metamaterials based on generalised viscoelastic modelling. *International Journal of Solids and Structures*, 126:163–174.

[46] Reggio, A., De Angelis, M., and Betti, R. (2013). A state-space methodology to identify modal and physical parameters of non-viscously damped systems. *Mechanical Systems and Signal Processing*, 41:380–395.

[47] Wua, X., He, H., and Chen, G. (2019). A new state-space method for exponentially damped linear systems. *Computers and Structures*, 212:137–144.

[48] Wagner, H. (1925). Über die entstehung des dynamischen auftriebes von tragflüge. *ZAMM - Journal of Applied Mathematics and Mechanics/Zeitschrift für Angewandte Mathematik und Mechanik*, 5:17–35.

[49] Theodorsen, T. (1935). General theory of aerodynamic instability and the mechanism of flutter. *TR496, NACA*.

[50] von Kármán, T. and Sears, W. R. (1938). Airfoil theory for non-uniform motion. *Journal of Aeronautical Sciences*, 5:379–390.

[51] Fung, Y. C. (1993). *An Introduction to the Theory of Aeroelasticity*. Dover Publications, New York, USA.

[52] Bisplinghoff, R. L., Ashley, H., and Halfman, R. L. (1996). *Aeroelasticity*. Dover Publications, Cambridge, Massachusetts.

[53] Arena, A., Lacarbonara, W., and Marzocca, P. (2013). Nonlinear aeroelastic formulation and postflutter analysis of flexible high-aspect-ratio wings. *Journal of Aircraft*, 50(6):1748–1764.

[54] Arena, A., Lacarbonara, W., Valentine, D. T., and Marzocca, P. (2014). Aeroelastic behavior of long-span suspension bridges under arbitrary wind profiles. *Journal of Fluids and Structures*, 50:105–119.

[55] Krushynska, A., Kouznetsova, V., and Geers, M. (2016). Visco-elastic effects on wave dispersion in three-phase acoustic metamaterials. *Journal of the Mechanics and Physics of Solids*, 96:29–47.

[56] Vadalá, F., Bacigalupo, A., Lepidi, M., and Gambarotta, L. (2021). Free and forced wave propagation in beam lattice metamaterials with viscoelastic resonators. *International Journal of Mechanical Sciences*, 193:106129.

[57] Brillouin, L. (2003). *Wave propagation in periodic structures: electric filters and crystal lattices*. Courier Corporation, Mineola, New York.

[58] Main, J. A. and Krenk, S. (2005). Efficiency and tuning of viscous dampers on discrete systems. *Journal of Sound and Vibration*, 286(1-2):97–122.

[59] Gattulli, V., Potenza, F., and Lepidi, M. (2013). Damping performance of two simple oscillators coupled by a visco-elastic connection. *Journal of Sound and Vibration*, 332(26):6934–6948.

[60] Kariyado, T. and Hatsugai, Y. (2015). Manipulation of Dirac cones in mechanical graphene. *Scientific Reports*, 5(1):1–8.